Department of Precision and Microsystems Engineering

Graphene deposition on MEMS devices

J. C. Rietveld

Report no	MNE 2017.036
Coach	A. Gkouzou
Professor	W.M. van Spengen
Specialisation	Micro and Nano Engineering
Type of report	Master of Science Thesis
Date	23 August 2017

TU Delft
Delft University of Technology
Challenge the future

Abstract

MEMS devices are currently designed to avoid sliding and contacting parts due to friction and adhesion problems. In this work, the possibility to grow a low friction material locally on MEMS sidewalls is investigated. An overview of the lubricants proposed in the literature for the microscale is presented, and graphene is selected as a promising and appropriate material for MEMS lubrication. Until now graphene is often transferred to surfaces, but for MEMS purposes a transfer step is not always possible. Chemical vapor deposition is selected as the appropriate technique for depositing graphene directly on MEMS sidewalls. In the deposition experiments, graphene is deposited using hydrogen, methane, a nickel catalyst, and a high temperature through Joule heating. The number of graphene layers and the quality of graphene is assessed by micro-Raman spectroscopy. The experiments revealed that it is possible to deposit graphene locally on the top and sidewalls of MEMS structures. The results of this report can be used for further research into graphene lubrication on MEMS surfaces, and it contributes to the development of a new field of MEMS devices with sliding and contacting structures with reduced friction and wear.

Contents

I Literature review: Lubrication of MEMS devices **4**

1 Introduction **5**
1.1 Thesis outline . . . 6

2 State of the art **7**
2.1 Vapor Phase Lubrication . . . 7
2.2 Self-assembled monolayers . . . 7
2.3 Hydrogen-terminated silicon layer . . . 8
2.4 Hexagonal Boron Nitride . . . 9
2.5 Molybdenum Disulfide . . . 9
2.6 Tungsten disulfide . . . 9
2.7 Diamond-like carbon . . . 10
2.8 Boron doped ultrananocrystalline diamond . . . 10
2.9 Graphite . . . 10
2.10 Graphene . . . 11
2.11 Conclusion . . . 11

3 Graphene production techniques **12**
3.1 Mechanical Exfoliation . . . 12
3.2 Unzipping carbon nanotubes . . . 13
3.3 Arc Discharge . . . 14
3.4 Epitaxial growth on silicon carbide . . . 15
3.5 Reduction of graphene oxide . . . 16
3.6 Chemical vapor deposition . . . 17
3.7 The ideal technique for *in situ* MEMS lubrication . . . 18

4 Chemical vapor deposition **20**
4.1 Catalyst . . . 20
4.2 Gases . . . 20
4.3 Pressures . . . 21
4.4 Heating . . . 21
4.5 Cooling . . . 22
4.6 Time . . . 22
4.7 Pretreatment . . . 22
4.8 Post treatment . . . 22
4.9 Process parameters for CVD of graphene on MEMS sidewalls . . . 23

5 Conclusions **24**

II Method **26**

6 Experimental setup **27**
6.1 Pyrometer . . . 28
6.2 Turbopump . . . 28
6.3 Probe station . . . 29
6.4 Gases . . . 29

6.5 Electrical circuit . . . 29

7 MEMS structures **31**
7.1 Fabrication process . . . 31
7.2 Structure design . . . 31
7.3 Nickel layer . . . 31

8 Experiments **33**
8.1 Procedure . . . 33
8.2 Variables . . . 34
8.3 Graphene characterization . . . 34

9 Micro-Raman spectroscopy **35**
9.1 Working principle . . . 35
9.2 Characterization of graphene . . . 36
9.2.1 Deviation in the Raman spectra . . . 36
9.2.2 Number of layers . . . 37

III Results **39**

10 Experimental results **40**
10.1 Graphene coverage on nickel structures . . . 40
10.2 Influence of temperature on coverage . . . 43
10.3 Influence of cooling time on coverage . . . 44
10.4 Influence of heating time on coverage . . . 44
10.5 Influence of post annealing on coverage . . . 44
10.6 Influence of alternating current on coverage . . . 46

11 Discussion of the results **47**
11.1 Die-dependent coverage . . . 47
11.2 Post annealing . . . 47
11.3 Electromigration . . . 48
11.4 Limitations of micro-Raman spectroscopy . . . 48

IV Conclusions **49**

12 Conclusions and recommendations **50**
12.1 Conclusions . . . 50
12.2 Recommendations . . . 51

V Appendix **i**

A Mask designs of the dies **ii**

B Raman response of structure C.5 **iii**

C Table with experimental details **v**

D Setup details **viii**

Part I

Literature review: Lubrication of MEMS devices

Chapter 1

Introduction

Micro-electromechanical systems (MEMS) are miniature devices with mechanical and electrical components. MEMS devices are in the range of a micron to a millimeter in size, and they comprise sensing, processing, and actuating elements. There are numerous applications where MEMS can be used, for instance in the automotive, aerospace, biotechnology, energy-harvesting, and consumer electronics industry. MEMS devices are made by means of microfabrication that can involve the deposition of structural and sacrificial layers on top of a silicon substrate, pattern transfer by means of lithography, etching of structural and sacrificial layers, and the final release of structural layers.

MEMS may consist of moving parts, such as cantilevers, springs, and sliders. When MEMS structures are in close proximity to one another, they can experience adhesion. If the structures are subject to sliding contact friction will restrain their relative motion. The reason behind these effects lies in the large surface-to-volume ratio of MEMS. Inertial forces are small, but the surface forces are significant. Contacting surfaces can stick because of the adhesion that can be caused by attractive surface forces. This can can result in device failure. Moreover, MEMS can experience wear caused by friction. When sliding surfaces are involved, surface roughness becomes more crucial; MEMS can have rough sidewalls resulting from the etching steps occurring during microfabrication. The asperities that compose the surface topography can interlock into one another, can experience high stress, and can prevent motion during sliding (Figure 1.1). For the motion to continue, these asperities have to be sufficiently deformed, or they can break given the brittleness of silicon. Upon breaking, wear debris particles (also sometimes called third-body particles) are introduced to the sliding interface, and they can contribute to even more wear. As a result, the damage to the device becomes irreversible. An example of a worn-out device is shown in Figure 1.2, where the pin and the hub of a MEMS engine come into contact with a gear. After a large number of sliding cycles, the engine fails. Wear debris particles are evident at the contact points. In addition to the wear particles, the sliding surfaces conform more to one another; therefore, they are prone to adhesion, since the real area of contact will have increased. Hence, the sliding surfaces will adhere more easily to each other, and the device's components can end up stuck.

One solution to the adhesion problem might be to decrease the real contact area through increased surface roughness. Another solution is to lower the surface energy by chemically modifying the contacting surfaces. With regard to macroscale friction, the commonly used solution is to apply lubrication oil or grease between sliding surfaces. However, MEMS are microscale devices, and the oil-based lubricants can cause problems linked to high viscosity. It appears that solutions pertaining to surface passivation or the deposition of a low-friction material are desirable for MEMS lubrication purposes.

Since devices with sliding and contacting parts fail, most MEMS devices are currently designed to avoid contacting parts altogether. However, devices with moving parts, like gears and motors, seem to hold the key to more exciting applications. Unfortunately, such devices will not become commercially available if the lubrication problems are not solved. In this report, we will investigate the possible lubrication materials and methods, and we shall select one that is appropriate for MEMS devices. Then, we will explore the production techniques of this material, and we will choose the appropriate one for *in-situ* MEMS lubrication.

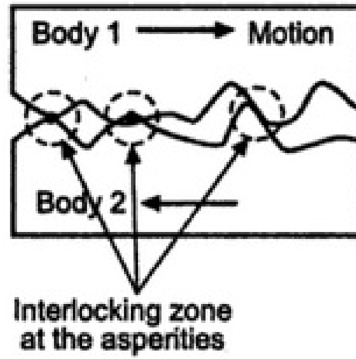

Figure 1.1: Asperity interlocking of two opposite surfaces that are subject to sliding contact. The locking mechanism prevents motion; the motion will continue once the asperities have been sufficiently deformed or worn out [1].

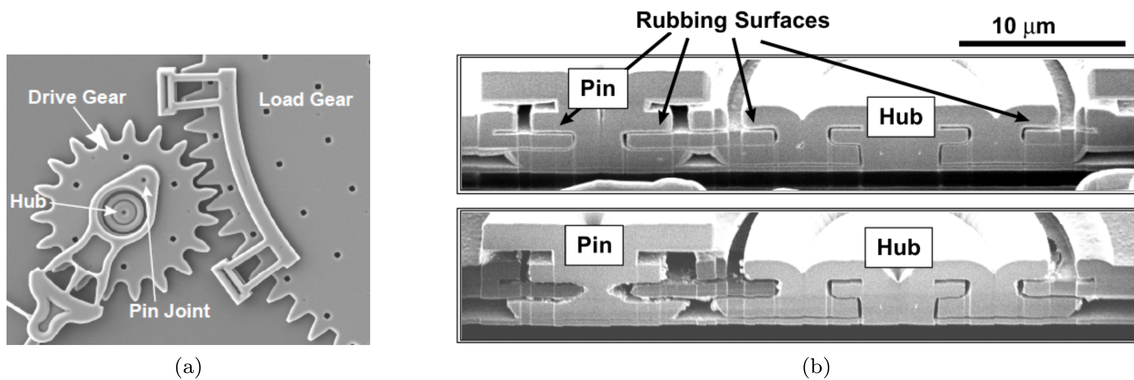

(a) (b)

Figure 1.2: The pin (joint) connects an actuator to the drive gear. The hub is anchored to the substrate. The pin rotates when the gear turns around the hub. (a) A top view of the gears and joint. (b) A cross section of the pin and hub. The top figure shows no debris, but after 480k cycles, there is failure and a lot of wear that is shown in the bottom figure [2].

1.1 Thesis outline

This thesis consists of five parts. Part I comprises the present chapter, and Chapters 2 through 5. In this part, I present the literature review on lubrication of MEMS devices conducted prior to my experimental work. In Part II, which comprises Chapters 6 through 9, I present the method we use, as well as experimental details concerning parameters, lab equipment, structure design, and characterization of the deposited material on the MEMS structures. Part III elaborates on the results achieved with our method. In particular, Chapter 10 introduces the outcome of several representative experiments, and how it is affected by varying several parameters. The next chapter, Chapter 11, discusses these results, and I present possible explanations on our observations in it. In Part IV, which comprises Chapter 12, I draw conclusions and give some recommendations for further research. The reader can find the appendices in Part V for more information on experimental details.

Chapter 2

State of the art

A lot of different materials can be used as anti-stiction coatings or hard coatings against friction and wear. Since we want to prevent failure of MEMS devices during their operation, we need lubricants that can be applied to the MEMS sidewall surfaces without the need for a liquid oil medium. Those lubricants must be long-lasting, since it is hard to replace them once they are worn out. There are several lubricants proposed in literature that protect from the friction and adhesion problems on the microscale. In this chapter, the state of the art in MEMS lubrication will be investigated. The appropriate lubrication material for MEMS devices will be selected.

2.1 Vapor Phase Lubrication

Vapor Phase Lubrication (VPL) is an *in situ* technique in which the molecules for lubrication are in a feed gas in the surroundings of a device. The molecules diffuse and adsorb to the surface of the device's components, and they form a protective layer. By controlling the pressure of the feed gas, the thickness of the protective layer can be varied [3]. The feed gas that consists of a mixture of nitrogen and acetylene will form a graphite layer on the surface [4]. Another possibility is to use a feed gas consisting of alcohol vapor in order to form an alcohol-based lubrication layer on the MEMS devices [5].

An advantage of this lubrication method is that it coats all the surfaces of a device entirely. Since capillary condensation forces the lubricant to the right places, hidden surfaces are covered too if the gap between surfaces is large enough for the molecules [3]. Another advantage is that the film that is created lubricates the surfaces continuously if the feed gas replenishes constantly. This provides a long lifetime to the device [6, 4]. Moreover, the layer is robust, and it has a low coefficient of friction (COF) [4].

A disadvantage of this type of lubrication is the risk of stiction due to increased adhesion. Molecules from the feed gas can condense and form capillary bridges between surfaces that are in close proximity with one another. Capillary bridges increase the adhesion force, which increases the likelihood of stiction. In contrast to a feed gas with water molecules, capillary forces resulting from a feed gas with alcohol molecules are negligible due to lower surface tension of alcohol [5]. Another disadvantage of this lubrication method is that some precautions have to be taken. When acetylene is used as the feed gas, an extra chamber is needed around the device for safety. The reason is that there is a risk of fire and explosion of acetylene at a high temperature [4]. Moreover, a sealing is required around the device to ensure a continuous concentration of feed gas around the device. The pressure of the feed gas has to be adjusted according to the temperature of the device. However, it can be difficult to control the pressure in a sealed device. When the pressure changes from the required pressure, the COF can increase [5].

2.2 Self-assembled monolayers

An assembly of organic molecules on a surface can form a monolayer. These molecules are chemically adsorbed to the surface through their polar head group [7, 8]. The layer that these molecules compose

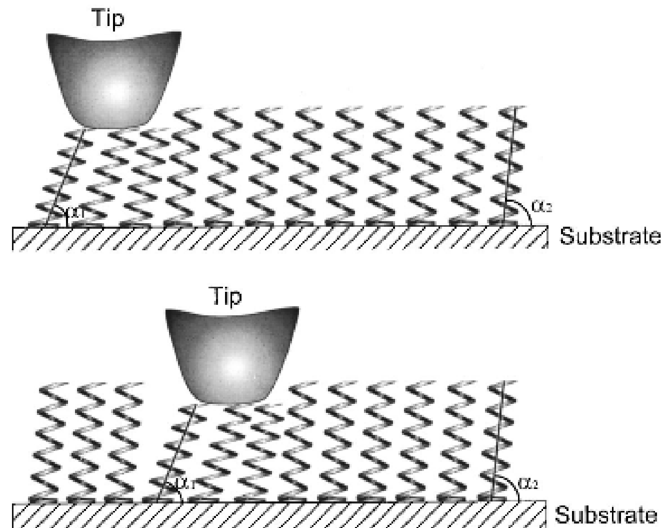

Figure 2.1: A molecular spring model of the self-assembled monolayer. The springs reduce the shearing force, which reduces the friction force [10]

is commonly referred to as a self-assembled monolayer (SAM). SAMs can eliminate stiction and reduce friction [7]. The lubrication efficiency is influenced by the packing density of the monolayer [3].

The carbon chains of SAMs can be modeled with springs (Figure 2.1). Because of the compliance of carbon chains in the layer, SAMs can have a very low COF and a good wear resistance [8]. SAMs are an attractive solution for solving adhesion problems related to the release of structures during microfabrication. Moreover, it is an attractive material for reducing the possibility of stiction of contacting surfaces during operation of a MEMS device [7].

A disadvantage of using the SAMs as a lubricant is that they wear-out during operation of the MEMS device. The layer wears off fast during sliding due to weak bonding to the surface, and this results in device failure [8]. The lubrication and anti-stiction coating will thus function only for a short time during sliding of the device's contacting components. Another disadvantage is that it is hard to replenish the layer [7]. When the layer is worn-out, a new layer has to be produced by a deposition technique. Moreover, the layer is not able to tolerate high temperatures [9]. This limits the use of SAMs to adhesion reduction in MEMS devices.

2.3 Hydrogen-terminated silicon layer

Hydrogen can passivate a silicon surface. The resulting layer can be used as an anti-stiction and lubrication coating. Hydrogen atoms terminate the dangling bonds of silicon atoms. Thus, hydrogen termination reduces the surface energy of the silicon surface, and it results in lower adhesion and friction forces between contacting and sliding surfaces, respectively [11].

An advantage of this method is that it is relatively simple; a wet chemical process is sufficient to passivate the silicon surface [12]. Moreover, the process can be made selective; it is possible to cover only a part of the surface with hydrogen. Furthermore, the passivated silicon layer is relatively inert and insensitive to humidity [13]. Hence, the devices with hydrogen-terminated surfaces can be used in various environmental conditions. It is also possible to replace the hydrogen atoms with a different type of atom, like nitrogen or oxygen. In this way, the silicon surface can have different properties [12].

Since hydrogen-to-silicon bonds are rather weak, the hydrogen layer is unstable. Therefore, the layer will quickly wear off during operation of a MEMS device [14]. Another disadvantage of this lubrication method is that it is not possible to passivate the complete surface. There will always be some remaining dangling bonds that can interfere with the chemical and electronic properties of the MEMS structures [15, 16]. When silicon is passivated by a wet chemical process, it will be very difficult to produce atomically flat surfaces. A treatment in ultrahigh vacuum can solve this issue [15].

2.4 Hexagonal Boron Nitride

Boron and nitrogen atoms can be arranged in a honeycomb structure to form hexagonal boron nitride (h-BN). The boron and nitrogen atoms are held together by covalent bonds. Van der Waals forces bind the layers of h-BN with one another. The layers shear easily because of weak Van der Waals forces [17, 18]. Therefore, h-BN has low friction. The h-BN layers that are stacked together can be used as a solid lubricant or as a lubricant additive [19, 20]. By increasing the number of h-BN layers, the COF can be reduced [21].

h-BN has a very high mechanical strength and a low COF, and it has a smooth surface. Moreover, it can tolerate high temperatures [19, 21, 22]. There are no dangling bonds on the surface that can lead to a reaction with another element. This makes the layer stable and a suitable lubricant under various environmental conditions.

The main disadvantage of h-BN is that it has a low lubrication lifespan. Furthermore, the COF increases rapidly when the load exceeds a maximum limit. This can be explained by the low hardness of the layer and the poor adhesion to the substrate. Therefore, the h-BN layer is removed when the surfaces are sliding against one another at high loads. As a result, the sliding bare surfaces wear out fast [20]. Another disadvantage is the difficulty to produce a high-quality layer of h-BN. There are always some defects and impurities introduced during the synthesis which can increase the COF [19, 22].

2.5 Molybdenum Disulfide

Molybdenum Disulfide (MoS_2) is a commonly used solid lubricant. It forms a thin lubrication layer when added between two sliding surfaces. When two surfaces slide, the MoS_2 layer flows plastically between them, and it reduces friction. MoS_2 has a low COF in dry air [23, 24].

An advantage of this material is the good lubrication at a high temperature, as well as the high hardness [25]. It is a widely used material, and it adheres very well to metals [23]. Another advantage is the decreasing COF with an increasing load on the surface.

A disadvantage of MoS_2 is that it is not stable in several environments. Contaminants adsorb easily on a MoS_2 layer, and they contribute to a higher COF. MoS_2 can oxidize in humid air. At low temperatures, this oxide layer deteriorates the lubrication properties of MoS_2. Moreover, the oxide layer is hydrophilic, so it adsorbs water molecules that further increase the COF [25]. The COF also increases at a decreasing temperature [25].

2.6 Tungsten disulfide

Tungsten disulfide (WS_2) is used as a solid lubrication. The structure of WS_2 resembles the one of MoS_2 [26, 27]. When one applies WS_2 to sliding surfaces, it forms a smooth film [28]. The lubrication property originates from the crystal structure. The S-W-S layers are bounded by weak Van der Waals forces. Therefore, the S-W-S planes shear easily [29].

An advantage of using WS_2 as a lubricant is that it can tolerate high temperatures and high pressures [30]. The smooth film which is formed on the surfaces during sliding, has a good adhesion to the substrate. Therefore, the lubricant has a long lifetime during operation of a MEMS device [29].

A disadvantage of WS_2 is that it can only be used in dry environments. It loses its lubrication properties in humid air because of oxidation [30]. WS_2 oxidizes to WS_3, which has a much higher COF [29]. Another disadvantage is that the COF increases with increasing temperature and humidity. This makes it hard to predict the friction forces and the wear resistance of a device coated with WS_2 [28].

2.7 Diamond-like carbon

Diamond-like carbon (DLC) is a hard coating that is commonly used due to its low COF and its mechanical strength. It is a hydrophobic amorphous carbon coating [31, 32]. DLC can be used as the device's structural material, or as a protective coating. By applying DLC as a protective coating, the operational lifetime of MEMS devices can increase [3, 32]. When hydrogen atoms bond with the carbon atoms of DLC, the surface energy decreases, which lowers the COF. However, hydrogen decreases the wear resistance, so it reduces the lifetime of the coating [32].

DLC has lots of attractive properties. It has a very small wear rate, it is mechanically strong and it has a low COF in dry air. Moreover it is unreactive to acids and alkalis, and it is stable up to a temperature of 600 °C [32, 7, 31]. Due to low surface energy, DLC is a good solution to the adhesion problems [32]. Another advantage is that one can make a uniform DLC coating. In addition, it follows the topography of the substrate offering excellent conformity [7].

DLC can have problems with high compressive stresses that cause delamination of the lubrication layer from the substrate. The energy of the ions that are used during the deposition determine the magnitude of the compressive stresses [32]. The delamination of DLC can damage the MEMS structures and can cause device failure [7]. Another disadvantage is that DLC needs high deposition temperatures that require high energy consumption. DLC also has poor adhesion to the substrate when used as a coating [32]. Although DLC is unreactive to acids an alkalis, these molecules can still influence the friction and the wear behavior by physical adsorption to the DLC surface [7].

2.8 Boron doped ultrananocrystalline diamond

Boron doped ultrananocrystalline diamond (B-UNCD) is a relatively new diamond-based material, that has a much smaller grain size than diamond [33]. The doping of ultrananocrystalline diamond with boron results in a conductive material with a low COF [34]. B-UNCD can be applied as a lubrication film on a substrate or as the structural material of a MEMS device [35].

An advantage of using B-UNCD as the structural material is the material's relatively long lifetime [35]. Moreover, it has a high hardness, a high Young's modulus and a very low wear rate [33, 34]. It has a low surface roughness and a low COF. In addition, it provides sliding surfaces with good wear resistance. Another advantage of B-UNCD is that the COF decreases when the load on diamond-to-diamond sliding surfaces is increased [34].

A disadvantage of B-UNCD is the limited contact force that can be applied in humid atmosphere. At high loads, a lot of damage can be induced to the sliding surfaces. The surfaces can also stick due to the capillary adhesion [35].

2.9 Graphite

Graphite is commonly used as a solid lubricant in various applications. Carbon atoms are structured in hexagonal planes with intermediate water molecules to achieve good lubrication properties. Therefore, graphite is the perfect material to be used as a lubricant in humid air. Graphite planes shear easily because of the reduced binding energy among them [36]. Graphite forms easily flakes because of the weak binding. The flakes can generate third body particles between the sliding surfaces, offering a carbon-based tribofilm against friction [37].

Graphite can be used in high-temperature applications up to 450 °C . Other advantages of using graphite as a lubricant are the low cost, the good lubrication performance, and the low wear rate [17]. Moreover, graphite is unaffected by pressure differences. When one reduces the pressure that surrounds the graphite layer, it will not change its COF [36, 38]. Another advantage is the restoring property of graphite. When a structure is sliding at a high load, we can maintain a low COF by adding oxygen. The oxidation of graphite smoothes the surface, and it reduces the COF [39].

Since water molecules are required to have a low COF, graphite cannot be used as a lubricant in high vacuum. Therefore, device packaging can be a limiting factor when using graphite as a solid lubricant on the structures. Moreover, it is difficult to constantly have water molecules at the sliding interface.

2.10 Graphene

Graphene was first isolated from bulk graphite by mechanical exfoliation [40], and later studies focused on more production techniques. Graphene is a two dimensional material. Single-layer graphene consists of one atomic carbon layer, while few-layer graphene consists of a few atomic layers of graphite. Just like graphite, the lattice of graphene has a hexagonal honeycomb structure. Graphene has unique and impressive mechanical properties. The number of graphene layers, the production method of graphene, and the substrate that is coated with graphene influence the material's friction properties [41]. Graphene can be used as a lubrication film or as an additive to lubrication oils.

Advantages of graphene are the exceptionally high strength, the high shear, and the high stiffness. Moreover, graphene has an atomically smooth surface [40, 42]. Another advantage is that graphene is a good lubricant in both dry and humid air. It is possible to replenish a graphene layer by sufficiently reheating the layer under a hydrogen atmosphere when carbon atoms are in the substrate. Compared to graphite, graphene provides a better protection against wear [40]. The COF can decrease with an increasing number of graphene layers, up to four layers [41]. Another advantage is that graphene can act as a passivation layer on the surfaces that react chemically with surrounding molecules. For example, a graphene layer can prevent the corrosion of metal surfaces [40].

A disadvantage of using graphene is that the COF is influenced by the environment. Defects, chemical modifications, and oxidation of the surface increase its COF. Moreover, in humid air, graphene layers have to be replenished to ensure low friction and wear [40].

Superlubricity is the state in which two surfaces slide with zero or very little friction due to lattice mismatch [43]. In a recent study, Berman *et al.* achieved macroscale superlubricity by sliding a graphene-coated silicon dioxide surface against a DLC ball with nanodiamond particles as an additive [44]. They also performed mesoscale molecular dynamic (MD) simulations and came up with interesting results.

In their simulations, superlubricity is achieved by the incommensurability between a block of DLC and several graphene patches. The graphene patches scroll over some nanodiamond particles, and they consequently form rolls with the nanodiamond. This results in a reduced real area contact. The contact between the multiple graphene patches and the nanodiamond particles resembles a multi-asperity contact, similar to the one found in MEMS; MEMS can have rough sidewalls, which, when in contact, can form a multi-asperity system. Therefore, superlubricity can be presumably achieved when a graphene layer is grown on the sidewalls of MEMS devices, as long as the opposite graphene layers form an incommensurable contact.

2.11 Conclusion

In this chapter, the state of the art in MEMS lubrication was investigated. We will select graphene as a lubrication material for MEMS, because it is appropriate to both dry and humid air, in which the MEMS devices operate. Furthermore, it is possible to replenish the graphene layer. Moreover, graphene has excellent mechanical and lubrication properties, which make it the most attractive material for the lubrication of MEMS.

Chapter 3

Graphene production techniques

Graphene can either be produced by top down processes, from graphite or carbon nanotubes, or by bottom up processes, from single carbon atoms. In this chapter, we will consider the different techniques and regard the graphene quality, the cost-effectiveness, and the possibility of large-scale production. Finally we select the most suitable production technique for the local deposition of graphene on MEMS sidewalls.

3.1 Mechanical Exfoliation

The most popular mechanical exfoliation technique is 'the scotch tape' method. The graphene layers are peeled off from a graphite block. By repeatedly peeling off the layers of the tape, all that remains is a structure that resembles graphene (Figure 3.1). Graphene flakes up to 10 micron in size can be extracted, and their size is determined by the grain size of the graphite [45] Another mechanical exfoliation technique is the wedge-based one, where the layers are scrapped from the graphite with an ultra-sharp diamond wedge.

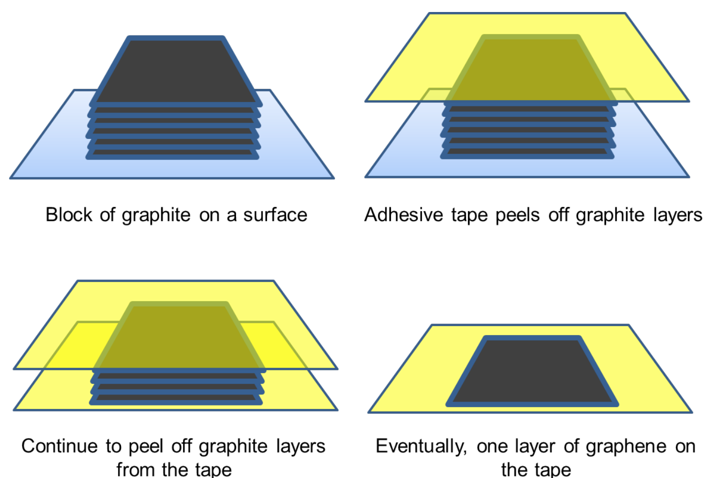

Figure 3.1: The basic process of mechanical exfoliation with scotch tape. By repeatedly peeling off layers from graphite, one can obtain graphene, which can be of a single layer.

The main advantage of the exfoliation method is that it is a straightforward graphene production technique, though rather labor-intensive. Another advantage is that the obtained graphene film is monocrystalline [21]. Moreover, the quality of the produced graphene can be high when the graphite block is of high quality [46].

The resulting graphene can be used for fundamental research only since the size of the flakes is difficult to control. Another disadvantage of this method is the difficulty for large-scale production. Moreover,

it is hard to reproduce graphene of the same quality and size [21]. Another disadvantage is that the graphene film needs to be transferred from the tape or wedge to a substrate. Therefore, this method is not easily applicable to the MEMS case, since the transfer of graphene from the tape or wedge to the MEMS sidewalls might destroy the graphene and the device.

3.2 Unzipping carbon nanotubes

A carbon nanotube (CNT) is a graphene sheet rolled up into a tube. To obtain graphene sheets, the CNTs are cut and unraveled. The cutting or tearing of CNTs is done by making use of a chemical or mechanical method. The tearing must occur longitudinal and linear for a neat graphene sheet. There are different methods to unzip CNTs. One can use a chemical reaction to break the bonds by putting the CNT in a solution of concentrated sulphuric acid (H_2SO_4) and potassium permanganate ($KMnO_4$). The CNT is then heated and oxidized, and the unzipping takes place from an initial opening along a line [47]. The basic process is shown in Figure 3.2a. Another method is covering the surface of the CNT with polymethyl methacrylate (PMMA) and leaving a small strip uncovered. Afterwards, the top surface of the CNT is etched with argon plasma, which will react along the uncovered straight line [48]. A third method to unzip the CNTs is by sequential hydrogen plasma-assisted etching and a subsequent passivation process to avoid damage of the sidewalls. Those sequences can be repeated until the CNT is satisfactorily unzipped [49]. The process is shown in Figure 3.2b. Another method to produce graphene from CNTs is the high impact method. CNT arrays in a clump are shot at hypervelocity on a solid target (Figure 3.2c). The carbon bonds will break longitudinally due to high stress [50].

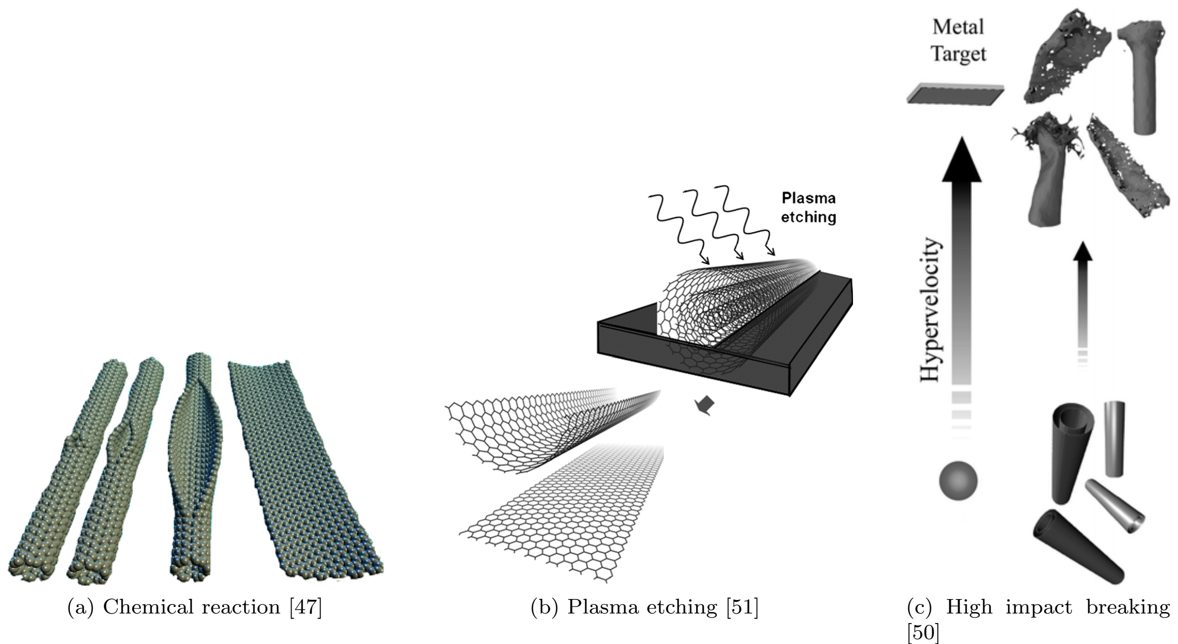

(a) Chemical reaction [47]

(b) Plasma etching [51]

(c) High impact breaking [50]

Figure 3.2: Carbon nanotube unzipping method schemes.

An advantage of the unzipping process is that it is a direct way of obtaining graphene, because the CNT needs to be cut or unzipped. The quality of the graphene can be very high when using a high-quality CNT. Moreover, an advantage is that the unzipping process can be controlled when using a chemical unzipping method, which results in graphene sheets with relative smooth edges [48, 52, 49]. An advantage of unzipping with the high impact method is that it does not need chemicals, although it does need a system to bring the CNTs to hypervelocity. Depending on the unzipping method, the process can be of low cost and of high speed [50].

The chemical unzipping method can be complicated. It requires some precautions to ensure that the cut is in a straight line, as well as to prevent reassembling of the tube or curling of the sides. In addition, it is very likely that single-walled CNTs get twisted, so multi-walled and less compliant CNTs are more preferable to unzip [47]. Moreover, the edges of the graphene sheets can get contaminated with residual

chemical groups. They can be removed with an extra chemical reaction or by heating. The plasma etching unzipping must also be done with care to minimize the damage on the sidewalls of the graphene sheets. Not all CNTs can be unzipped with this etching method, some CNTs overlap with other CNTs during unzipping [49]. Another disadvantage is the irregular surface structure. Therefore, the unzipping can be expensive when a high quality graphene sheet is desired. A heat treatment up to 2500 °C can eliminate defects on the graphene structure [52]. A disadvantage of the high-velocity impact method is that there is no control under what angle the CNTs clash against the target. Therefore, the breaking process is not repeatable. Moreover, not every CNT is unzipped successfully [50]. An obvious disadvantage of CNTs unzipping is that the graphene sheets need to be transferred to the MEMS sidewalls. It is not possible to produce the CNT directly on the place where the graphene layer eventually should be, and to proceed then with the unzipping process. Therefore, this method is not easily applicable for MEMS lubrication.

3.3 Arc Discharge

The electric arc discharge method uses two graphite electrodes in a water-cooled chamber [53]. A high current flows through these electrodes, and, once they are close together, discharge takes place. Graphite evaporates and forms a plasma at the center of the generated arc. The electrodes are kept at a constant distance. A buffer gas, such as hydrogen or helium, is used to prevent the graphene from agglomerating and from getting a closed structure similar to a CNT [53, 54, 55]. A schematic is shown in Figure 3.3. Arc discharge is a continuous process at a high pressure, a low voltage, and a high current [56]. The deposition of few-layer graphene takes place inside the whole chamber, but only the graphene that covers the wall is collected due to its higher purity, by scraping or washing it from the chamber walls [53, 54].

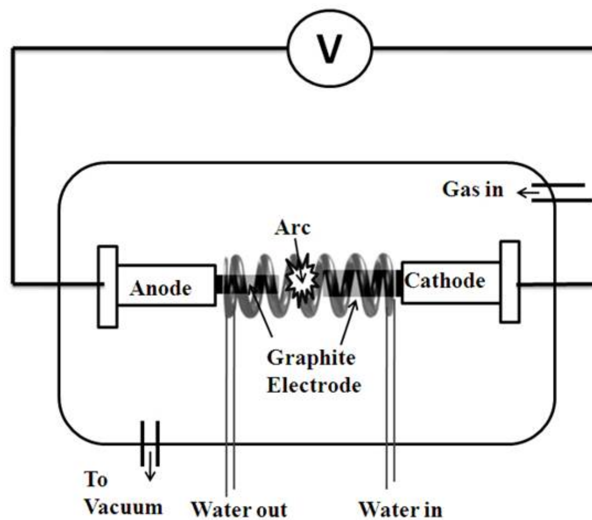

Figure 3.3: The principle of the arc discharge method. A high current flows through the cathode and anode. Arc discharge takes place and graphite evaporates at the center. [57].

The main advantage of this method is the high time efficiency. Grams can be produced in a few minutes. Moreover, it is suitable for large-scale applications and it is a relatively safe and an inexpensive method. In addition, no special substrate or catalyst is needed for the synthesis. Contrary to several chemical methods, there are fewer functional groups present on the graphene layers. The buffer gas determines the purity and the quality of the graphene produced [56, 46, 53].

A disadvantage of this method is that the graphene surface is not perfectly smooth. The surface of the produced graphene can have wrinkles and some defects [56]. Another drawback of this method is that it is not very efficient, since only a small amount of the graphene that is produced is collected, excluding for example the graphene produced on the electrodes due to the presence of other particles [54, 53]. A huge disadvantage of the arc discharge method is that the graphene cannot be directly produced on a substrate. A transfer from the chamber walls to the substrate is always needed, so it is difficult to deposit graphene very locally on the MEMS sidewalls with sufficient coverage.

3.4 Epitaxial growth on silicon carbide

The epitaxial growth of graphene on silicon carbide (SiC) can be performed under vacuum conditions or in an argon atmosphere close to atmospheric pressure [58]. The SiC substrate is heated until the silicon sublimates. The carbon remains on the substrate, and it forms an epitaxial graphite layer [59, 60]. The basic process is shown in Figure 3.4. The graphene can be grown on the Si-face and the C-face of silicon carbide (Figure 3.5). For the uniformity and the control on the number of graphene layers, it is important to use the corresponding surface of SiC. On the C-face, it is much more difficult to control the growth than on the Si-face [61, 62]. The temperature needed for the sublimation of silicon is 1500 °C in the argon atmosphere and at 1 bar, while in an ultrahigh vacuum condition the temperature is 1000 °C [58, 61]. The time of heating and the sublimation temperature affect the number of graphene layers that are grown [63]. Temperature influences the graphene structure, since high temperatures lead to annealing of the surface and to a better surface morphology [58].

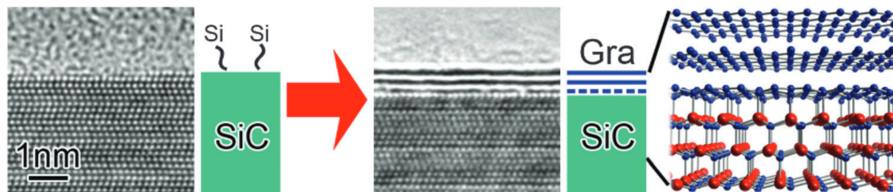

Figure 3.4: The principle of the epitaxial graphene growth on silicon carbide. The substrate is heated until silicon sublimates. The carbon remains on the substrate and forms graphene layers [64].

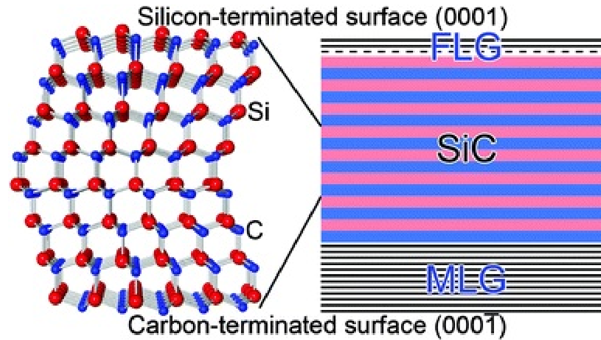

Figure 3.5: The two faces of silicon carbide. The red dots and lines correspond to silicon and the blue ones to carbon. Few-layer graphene is produced on the silicon face and multi-layer graphene is produced on the carbon face [64].

An advantage of the graphene growth on SiC is that it can be carried out on a large scale. Furthermore, the graphene can directly grow on a SiC substrate. When we fabricate a MEMS using SiC as the structural layer, and we perform the epitaxial graphene growth in argon atmosphere, the graphene will be synthesized directly on the MEMS components. The graphene will be of high quality, and it will provide a homogeneous covering. Compared to graphene produced under vacuum conditions, the quality of graphene produced under argon atmosphere is much better [58, 61].

The epitaxial growth on SiC is an expensive method, since SiC is an expensive material. Another disadvantage is that only small grains (30 – 200 nm) of graphene are obtained under vacuum conditions [58]. Due to deep pits that can form during the synthesis, the layer has bad homogeneity and high roughness [65]. To prevent this, a higher temperature and fast heating can be applied, but this may result in a higher nucleation density [62, 61]. The number of layers grown is difficult to control, especially in large-scale production. The silicon will continue to sublimate, resulting in non-self-terminating graphene layers. This can lead to different graphene thicknesses between regions on a substrate. Moreover, there is a challenge in the control of the graphene growth patterns when using the C-face of SiC [63, 58].

3.5 Reduction of graphene oxide

The basic process from graphite to graphene by oxidation, exfoliation, and reduction starts with a substrate of graphite (Figure 3.6). The substrate is oxidized through a combination of potassium permanganate, sodium nitrate, and sulfuric acid. This process is known as the Hummers method [66, 67]. To get single-graphene sheets, the graphite should be completely oxidized [68]. Afterwards, the graphite oxide is exfoliated. Because of the oxidation, water molecules are introduced between the sheets of graphite oxide, that increase the space among them. This weakens the interaction between the sheets and it facilitates their exfoliation. When using sonication or mechanical stirring in water, the sheets can be completely exfoliated, resulting in graphene oxide (GO) sheets [67, 69, 70]. Graphite oxide can also be exfoliated by rapid heating; a gas, such as CO_2, can be introduced between the sheets of graphite oxide. Due to the difference in thermal expansion between the sheets and the gas, the heating will lead to the exfoliation of the sheets [68, 46].

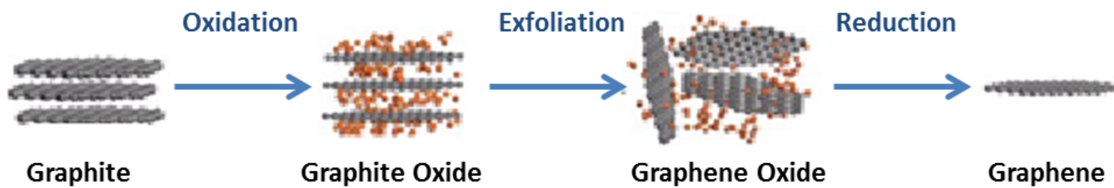

Figure 3.6: The principle of obtaining graphene from graphite by oxidation, exfoliation, and reduction [71].

The reduction of graphene oxide can be carried out in four different approaches. The first method is the chemical reduction with a reducing agent, such as hydrazine. The hydrazine is added to the solution with the GO sheets, and the mixture is heated up to 100 °C. The graphene will aggregate during reduction [63, 72, 70, 69, 73]. The second method is the thermal reduction. At high temperatures and under high vacuum conditions, or at low temperatures and in an ionic solution, the oxygen is removed from the GO sheets [73, 67]. Afterwards, the product can be hot pressed in vacuum [74]. The third method, the photocatalytic one, uses UV radiation to reduce the GO that is in a solution with ethanol [75, 46]. The last method is the electrochemical reduction. There are two different techniques in which this method can be employed. The first technique is the direct reduction of the GO in a non-hazardous buffer of electrolyte at room temperature. A potential is applied between the two electrodes that are in the buffer to drive the reduction. The reduced GO deposits on the surface of one of the two electrodes that acts as the working electrode. The second technique is the indirect reduction of GO sheets. The sheets are first deposited as a film on a substrate. The substrate will subsequently act as the working electrode. Similarly to the first technique, a buffer is required. The GO sheets are reduced using a three-electrode electrochemical system [67].

An advantage of this method is that it is scalable and it is suitable for large-scale production. The exfoliation to individual GO sheets is also relatively easy. The individual sheets remain stable in the solution, and they will not re-stick to the graphite oxide. Moreover, they have a uniform thickness [69, 70]. A benefit of the chemical reduction method is that it is an energy-efficient technique [63]. The thermal reduction method can also be energy-efficient, since it can be carried out at low temperatures when using an ionic solution [73]. Hot pressing is a treatment that applies a high temperature (500 – 1500 °C) and an uniaxial pressure (5 – 40 MPa) to materials. It is an effective treatment to improve the quality of graphene, because the defects and the functional groups are completely removed [74]. An functionality provided by the photocatalytic method is the possibility to produce the graphene selectively. By making use of a mask, specific locations of the substrate are radiated with UV and subsequently reduced to graphene [46]. With regard to the electrochemical method, an advantage is that it is fast and environmentally friendly because safe electrolytes can be used [72]. Moreover, the process can be done at room temperature, and the user has control on the potentials. Finally, the technique is recommended for large-scale production of graphene [67, 46, 67].

A disadvantage of this method is that there are always structural defects left after the reduction [63]. A drawback of the thermal exfoliation technique is that the sheets can get wrinkled [46]. As for the chemical

method, a disadvantage is that it produces toxic waste. The chemical reducing agent is often very harmful to the environment, and, in addition, it may contaminate the produced graphene [67]. Nevertheless, there are some environmental-friendly reducing agents, like vitamin C and aluminum powder, but they can absorb on the graphene surface and change the properties [76, 77, 78, 63]. The photocatalytic method has the drawback that photoactive materials are required for the reaction [79]. The thermal method has cost-related disadvantages due to the high temperatures, and it is hard to control the reduction, as the temperature is the only key variable [80, 67]. Another disadvantage is that there are always some oxygen groups left [68]. The electrochemical method struggles with the same problem of residual oxygen and defects [67]. The main disadvantage of the reduction of graphite oxide is that the graphene cannot be produced locally on the MEMS sidewalls. The graphene is in a solution, and it needs to be spin-coated on the surface in question. Therefore, it is not easily applicable for the MEMS lubrication purposes.

3.6 Chemical vapor deposition

Chemical vapor deposition (CVD) is a popular method for the production of single-layer and few-layer graphene. The process requires a catalyst like nickel [81], copper [82], germanium [83], or platinum [84], and it needs a hydrocarbon gas, like methane, as a carbon source. The process with a nickel catalyst is illustrated in Figure 3.7, and the process with a copper catalyst is illustrated in Figure 3.8. At high temperature, the hydrocarbon gas decomposes and the carbon atoms diffuse into or adsorb on the surface of the catalyst [85]. The number of graphene layers formed depends on the type of catalyst, the type and ratio of the gases, and the temperature [46].
Plasma-enhanced CVD (PECVD) can also be used for the production of graphene. The method is the same as for CVD, but instead of heating it uses a plasma source that supplies the energy needed for the reaction. The plasma can be produced by means of a radio frequency technique [86, 46, 87].

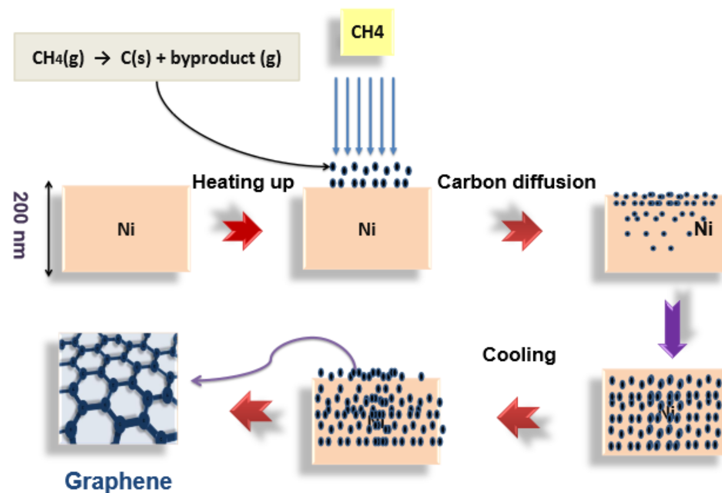

Figure 3.7: Chemical vapor deposition of graphene on a substrate of nickel [88].

CVD is the preferred method because the graphene grown with CVD is of a high quality, has a uniform surface, and low defects [82, 85, 46]. Moreover, it can produce millimeter-size graphene flakes. CVD is a flexible method, that is suitable for large-scale graphene production [90, 91, 21]. A great advantage of this method is that the graphene can be directly grown on the substrates covered with a catalyst or on a bulk catalyst. The catalyst can also be etched away so that the graphene can become freestanding and can be transferred to other substrates [46].
When using copper as a catalyst, the deposition of graphene is a surface-mediated process [90]. Carbon atoms adsorb on the copper surface but do not diffuse to the substrate, because carbon has a low solubility in copper [83]. When the copper surface is saturated, the carbon adsorption stops. Therefore, it is mainly single-layer graphene that is formed. Since the graphene production on copper is surface-terminated, the thickness of the catalyst has no influence on the graphene. Another advantage is that copper is a relatively cheap material. Carbon has a high solubility in nickel at high temperatures. The deposition of graphene using nickel is much faster than with copper [92]. Once the hydrocarbon gas has been decomposed, the

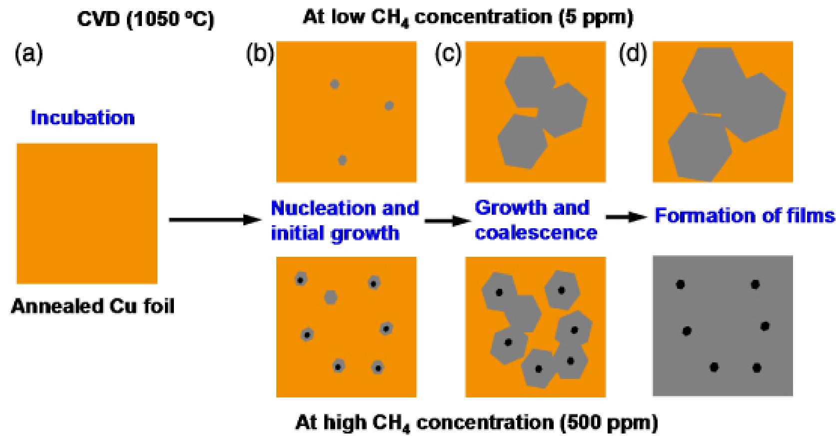

Figure 3.8: Cchemical vapor deposition of graphene on a substrate of copper [89].

carbon atoms diffuse in the nickel layer. By cooling to room temperature, the solubility of carbon in nickel changes, and the atoms precipitate to the surface. An advantage of using nickel as a catalyst is that the number of graphene layers can be low with a high cooling rate [82, 85, 90]. Furthermore, nickel is a relatively cheap catalyst. Moreover, an advantage is that the carbon atoms that remain in the nickel layer can act as a replenishment source. When reheating the layer in a hydrogen atmosphere, some new graphene layers can be produced. Nickel is the structural layer in MEMS devices fabricated with MetalMUMPs, a micromachining process that uses electroplated nickel [93]; thus, there exist MEMS devices that already have a nickel layer. The solubility value of carbon in platinum is between the one of copper and nickel. Therefore, carbon atoms both adsorb and diffuse in the platinum substrate. One advantage of using platinum as a catalyst is that a fast growth rate is possible when depositing at higher temperatures [94]. Moreover, the temperature during the process is far below the melting temperature of platinum of 1770 °C [95]. Germanium is both a semiconductor and a semi-metal. An advantage of using germanium is that it is possible to deposit a homogeneous, self-terminating layer of graphene by means of a surface-mediated process [83]. Another advantage is that germanium does not require any pretreatment [96].
In contrast to the CVD process, the PECVD process can be done not only when using transition metals as catalysts but also when using dielectric materials, though the graphene quality is then rather poor [97, 87]. However, the graphene produced by PECVD has only one to three layers of a high purity due to the lack of a catalyst or specific substrate [98, 99]. An advantage of PECVD relative to CVD is that there is no need to wait between the heating and the cooling [63, 86].

A disadvantage of using copper as a catalyst is that it can partially melt and sublimate during the CVD process. The maximum deposition temperature of 1000 °C is slightly below the melting temperature of copper which is 1084 °C [95, 100, 101]. The copper particles that are sublimated can contaminate the graphene produced [102]. A disadvantage of using nickel as a catalyst is that the produced graphene has small grain sizes and multiple layers because it is more difficult to control the number of layers with this catalyst than with copper [83]. A disadvantage of using platinum as a catalyst is that the material is expensive. In addition, platinum ruptures easily from the substrate when a thin film is applied due to dewetting during the graphene production [102]. A disadvantage of using germanium as a catalyst is that it is not commonly used for graphene production, and it is a relatively expensive material.

3.7 The ideal technique for *in situ* MEMS lubrication

The best production technique should be able to produce graphene layers locally on a MEMS surface. In this chapter, we have discussed the mechanical exfoliation technique, the unzipping of carbon nanotubes, the arc discharge method, the epitaxial growth on silicon carbide, the reduction of graphene oxide, and chemical vapor deposition.

One should keep in mind that the method of graphene production should be usable in large-scale applications. The reduction of graphene oxide, the epitaxial growth on silicon carbide, the arc discharge

method, and the chemical vapor deposition are all appropriate methods for large scale production.

An easy-to-implement method is preferred, because the industry will then be more likely to regard graphene as a realistic alternative against friction in the MEMS devices. The mechanical exfoliation method is the easiest method to produce graphene, because there is no need of a set-up, a carrier gases, or specific environmental conditions. However, the transfer to the MEMS sidewalls should be avoided, since it can lead to device damage. The chemical vapor deposition method and the epitaxial growth on silicon carbide are also relatively easy methods, since the substrate only has to be heated and cooled down under specific conditions.

Defects in the graphene structure and the morphology influence the tribological properties. It is preferred that the resulting graphene has a good uniformity and few defects. A wrinkled surface might even render the graphene sheets more rigid against stretching [91]. The mechanical exfoliation technique produces graphene of a very good quality. A drawback is that it is hard to reproduce the same flake size and quality using this technique. The method that unzips CNTs provides high-quality graphene sheets if the CNT that is used is also of a high quality. The epitaxial growth on silicon carbide forms graphene of a high quality if it is grown on the silicon face of silicon carbide. The arc discharge method synthesizes graphene with a quality that depends on the type of the buffer gas used. The reduction of the graphene oxide technique produces graphene of a moderate quality. The resulting graphene sheets will always have some structural defects, even if hot pressing is used. Finally, and most importantly, the chemical vapor deposition method provides high-quality graphene sheets.

The graphene must be grown *in situ* on the MEMS sidewalls and preferably not be deposited on another substrate and then be transferred to the sidewalls. The MEMS sidewalls are hard to access, because of the devices' size. The epitaxial growth on the silicon carbide and the chemical vapor deposition method are two techniques where the graphene can be grown directly on the MEMS surfaces without the need of a transfer step.

The materials and the environmental conditions, like temperature and pressure, determine the costs of the graphene production process. The cheapest method is the mechanical exfoliation technique where only one step is performed repeatedly to produce graphene from graphite in ambient air. The arc discharge method is a relatively inexpensive one, because only two graphite rods, a high current, and a chamber with the buffer gas is required. Still, not all the produced graphene can be used. The chemical reduction of graphene oxide is a low cost process too, because the substrate does not have to be heated, which depends on the type of reduction method that is used. However, chemicals are used for the oxidation and the reduction steps that can be expensive. Moreover, a lot of steps are involved. The epitaxial growth on the silicon carbide and the chemical vapor deposition method can be relatively expensive methods, because of the high energy consumption if an oven is used. Moreover, in the case of epitaxial graphene growth, silicon carbide is an expensive material.

To conclude, the most promising method for producing graphene for the MEMS lubrication is the chemical vapor deposition method. Since nickel is already used in the MEMS devices and since it enables multi-layer graphene growth, we will use a nickel catalyst. Although the CVD is not a low-cost technique, it is cheaper than the epitaxial growth on silicon carbide, and it is a relatively easy method that can produce the graphene directly on the surface. The resulting graphene is of a high quality, and the method is suitable for large-scale applications.

Chapter 4

Chemical vapor deposition

This chapter focuses on the chemical vapor deposition (CVD) of graphene on nickel. At a high temperature and in the presence of hydrogen and a catalyst, a hydrocarbon gas is decomposed into carbon and hydrogen. Carbon atoms diffuse into the catalyst and adsorb on the surface. When cooling, the carbon atoms form graphene layers on the surface. The catalyst reduces the activation energy that is needed for the hydrocarbon gas to decompose into carbon and hydrogen [103]. Various process parameters are discussed in this chapter in order to select the ones that match the local deposition of graphene on the MEMS sidewalls.

4.1 Catalyst

Carbon has a high solubility in nickel, and it diffuses into the nickel layer at a high temperature. During the process, it can also adsorb on the nickel surface [104]. Graphene is formed from the crystallization of the adsorbed carbon and from the precipitation of the diffused carbon during cooling. Carbon tends to nucleate on the grain boundaries of nickel [105, 92]. Therefore, the nucleation density depends on the number of grain boundaries of nickel. A single crystal layer of nickel does not have grain boundaries; therefore, there are limited sites where graphene can nucleate, if one does not take into account defects on the nickel layer that also trigger nucleation. Hence, graphene produced on single crystal nickel will in theory have a more uniform and a thinner layer of graphene compared to polycrystalline nickel [106, 85]. Polycrystalline nickel can have various diffusion rates of carbon along the surface, so the layer thickness of graphene is not uniform [107]. Because of the diffusion of carbon in nickel, the amount of hydrocarbon gas needed for the production of few-layer graphene depends on the thickness of the nickel catalyst [108]. Due to a difference in the thermal expansion coefficients of graphene and nickel, wrinkles can form. These wrinkles can increase the mechanical strength of graphene, and they can make it stiffer [91]. Moreover, higher mechanical strength can be achieved by having more chemical bonds between the grains of nickel and the grains of graphene. Therefore, the nickel should be polycrystalline when one wants to obtain graphene with a high mechanical strength [109].

4.2 Gases

Hydrocarbon gas is used as the carbon source for the graphene deposition. The hydrocarbon gases that are used for CVD of graphene are methane [105], acetylene [107], or ethylene. Of these gases, methane is the one most commonly used [108]. By increasing the amount of hydrocarbon, more carbon atoms are adsorbed on the surface, which subsequently increases the number of graphene layers. More hydrocarbon gas can accelerate the deposition of graphene [100, 110].

Graphene cannot be deposited in the absence of hydrogen. Hydrogen gas is a co-catalyst in the CVD process [100]. The hydrogen to methane ratio determines the graphene quality and the number of layers that can be deposited. It can passivate dangling bonds and defects and so it improves the quality [111]. Hydrogen can increase the production rate of graphene on nickel. Hydrogen atoms can resurface

Hydrogen (%)	Argon (%)	Methane (%)	Acetylene (%)	Reference
76	19	5	-	[109]
30	69.9	0.1	-	[101]
95.6	-	-	4.4	[107]
98.5	-	1.5	-	[82]
99 − 99.5	-	0.5 − 1	-	[105]

Table 4.1: Flow ratios found in literature.

and desorb from the nickel surface. Consequently, more sites become available for the hydrocarbon to decompose [112]. At higher concentrations, hydrogen can also etch away the deposited graphene [107, 110]. Thus, there is an optimum hydrogen concentration to deposit graphene, to ensure that it is not etched away. This concentration has to be compared with the hydrocarbon concentration to produce the required number of graphene layers [100, 109].

Argon can be used as a buffer gas when one wants to increase or decrease the hydrogen concentration, but one still wants to keep the total pressure constant with a fixed amount of hydrocarbon gas. Argon gas can also be used during cooling, since argon does not react with graphene [100, 104]. The various gas ratios that are found in literature are given in Table 4.1.

4.3 Pressures

Graphene can be produced both under atmospheric and vacuum conditions. The pressure used in the literature varies from 10^{-3} mbar [107], 10^{-2} mbar [110], 1 mbar [112], to 10^{3} mbar [100]. The pressure does not influence the quality of the graphene, but it does affect the scalability, uniformity, and production costs. Moreover, it affects the flake size of graphene. At low pressure, the scalability of the process is limited, the energy costs are high, and the graphene flakes are irregular [104, 111]. At atmospheric pressure, the scalability of the process is better, the energy costs are lower, and the graphene flakes are regular and can be millimeter size [111]. However, there are more impurities present at atmospheric pressure from the gases, which can reduce the graphene quality.

4.4 Heating

The synthesis of graphene by CVD takes place at a high temperature. For a nickel catalyst, the deposition temperature is in the range of between 460 °C and 1000 °C. Below 460 °C, both carbide and graphene phases form. Between 460 °C and 650 °C, the carbon does not diffuse in the nickel, and the graphene growth is surface-mediated. Above 650 °C, the carbon starts to dissolve into the nickel layer [108]. A temperature around 700 °C can be used in vacuum conditions, which can lead to a single layer of graphene with a lot of defects [108]. Graphene is commonly synthesized on nickel at 1000 °C, which is still far below the melting point of nickel which is 1453 °C [95, 103, 109]. This high temperature leads to the best graphene quality with the CVD process. Moreover, it produces only a few layers of graphene [107]. Since temperature influences the solubility of carbon in the nickel layer, the temperature required for carbon atoms that diffuse in the nickel layer can be extracted from a Ni-C phase diagram [107]. However, there exists some uncertainty regarding the number of carbon atoms that diffuse in the catalyst [92].

The process can take place in a hot-wall or a cold-wall CVD system. In a hot wall reactor the entire furnace, including the substrate and the reaction gases, is heated. The hydrocarbon can already decompose in the furnace in the gas phase, and carbon atoms can diffuse to the catalytic surface and adsorb on it [113, 114]. In a cold-wall reactor the substrate is locally heated. The hydrocarbon adsorbs and decomposes on the catalytic surface and carbon atoms adsorb and diffuse in the nickel layer. The growth mechanisms of graphene on nickel in a cold-wall reactor with a fast cooling rate can resemble the growth mechanism on copper, which can be surface-mediated [113, 111]. The control of the number of layers is easier than with a hot-wall CVD, and the quality is better since there are no reactions of particles in the gas phase which can contaminate the graphene surface [111].

Since the CVD process requires high temperatures, there are high energy costs involved in the production of graphene. The costs are especially high when a hot-wall CVD system is used to heat the substrate. However, a cold-wall CVD system only heats the stage of the substrate, which could reduce the energy costs. Moreover, we could deposit graphene locally by selectively heating only the MEMS sidewalls instead of the complete substrate through Joule heating, which could further reduce the energy costs. Joule heating is a process that can rapidly heat up and cool down the device by applying a voltage difference to the selected parts. It is a fast process if the structure size is small.

4.5 Cooling

The cooling rate is important when using nickel as the catalyst. Carbon diffuses in the nickel during the heating step. When cooling, the solubility of carbon in nickel changes, and there are a lot of carbon atoms that precipitate to the surface to form graphene [115, 116, 107]. Because the precipitation process is not in thermodynamic equilibrium, the nucleation sites of graphene are randomly distributed, so it can grow from different domains. Graphene layers from different domains can overlap during the growth process, thus resulting in layers with non-uniform thicknesses [117, 104]. The cooling rate determines the speed at which carbon atoms precipitate to the surface of the nickel. At a fast cooling rate, less carbon atoms precipitate and diffuse to the surface than at a slow cooling rate. This suppresses the formation of multi-layer graphene, which leads to the formation of single- to few-layer graphene [111]. Hydrogen etching can remove graphene layers that are produced, and it requires a minimum temperature of 850 °C [100]. Therefore, fast cooling reduces the time that the substrate is at the right temperature for etching, so it reduces the time for graphene being etched by hydrogen during cooling. The cooling rate used in the literature varies from 7 $°C\,min^{-1}$ [115], 50 $°C\,min^{-1}$ [103], 150 $°C\,min^{-1}$ [104], to 600 $°C\,min^{-1}$ [91], and all these rates can result in monolayer, bilayer, or few-layer graphene. The cooling rate is determined by the heating capacity, the cooling gases that can be used, and the rate at which the heating power is reduced. Before graphene is exposed to air it is important that it is cooled down to at least 400 °C. At temperatures higher than 400 °C, the graphene is non-uniformly etched by oxygen [101].

4.6 Time

The total heating time in combination with the temperature determine the amount of carbon atoms that are diffused in the nickel layer. When the heating stops, there is no more hydrocarbon decomposition. A longer heating time increases the uniformity of the graphene layer, as well as the number of layers [109, 107].The heating time found in the literature varies from 10 s [118], 30 s [109], 2 min [104], 5 min [82, 105], 7 min [109] to 15 min [107]. When the heating time is short, the growth mechanism can resemble the growth mechanism of graphene on copper. Graphene will then mainly grow through the adsorption and the diffusion of carbon atoms directly on the nickel surface, and the growth of graphene by carbon precipitation and diffusion to the surface will be limited [118].

4.7 Pretreatment

What can improve the graphene quality is an initial treatment before the actual CVD of graphene. An initial annealing step can clean the surface by removing the oxide and contaminants on the surface of the catalyst, and it can improve the crystallinity of the substrate by increasing the grain size [82, 85, 92]. At high temperatures, annealing using hydrogen can etch the graphene layers [104]. Table 4.2 shows the parameters that are used in the literature to anneal the catalyst.

4.8 Post treatment

After the CVD process, the structure of graphene can be changed by a post treatment of annealing with hydrogen only or in combination with argon. Some carbon bonds of graphene break during annealing and this can reduce the number of graphene layers [119]. Moreover, it can make the surface more uniform

Time	Temperature (°C)	Gases	Reference
20 min	800	Hydrogen	[82]
5 min	900	Hydrogen	[110]
20 min	900	Argon and hydrogen	[105]
30 min	1000	Hydrogen	[104]
30 min	1000	Argon and hydrogen	[117]
1 h	1000	Argon and hydrogen	[101]

Table 4.2: Process parameters for nickel pretreatment annealing found in literature.

Time	Temperature (°C)	Gases	Reference
5 min	1000	Hydrogen	[104]
10 min	450	Argon and hydrogen	[110]

Table 4.3: Process parameters for nickel post treatment annealing found in literature.

[117]. Table 4.3 shows a number of process parameters found in the literature to anneal graphene after deposition.

4.9 Process parameters for CVD of graphene on MEMS side-walls

In this chapter we have discussed the process parameters of CVD. Because methane is often used as the hydrocarbon gas, we will use this gas for the CVD of graphene. Hydrogen is needed for the reaction, but can etch away the graphene layers if the concentration is high. Therefore, argon can be used as the buffer gas to control the ratio of methane and hydrogen while producing at atmospheric pressure. The temperature required for the reaction is between 700 °C and 1000 °C, and the heat is provided through Joule heating for 30 s to 15 min. Since Joule heating will be used, the cooling rate can depend on the geometry of the device. No pretreatment or post treatment is needed, because the improvement in the quality of the graphene layer is not important for lubrication applications. The process parameters that we will review in our experimental work are shown in Table 4.4.

Gas ratio [%]	P [bar]	T [°C]	t [min]	CVD type	Reference
H_2:CH_4 = 99:1	1	1000	5	Hot wall CVD	[105]
H_2:CH_4 = 50:50	0.003 – 1	850	0.2 – 2	Cold wall	[120]
H_2:CH_4 = 98.5:1.5	1	1000	5	Cold wall	[82]
H_2:CH_4:N_2 = 12:1:87	0.01	1000	5	Cold wall	[118]
H_2:CH_4:N_2 = 12:1:87	0.03	1000	0.2	Cold wall	[113]
H_2:CH_4:Ar = 76:5:19	1	965	0.5 – 7	Hot wall	[109]
H_2:CH_4:Ar = 93:5:2	1	1000	2	Hot wall	[104]
H_2:CH_4:Ar = 20:16:64	1	1000	3 – 7	Hot wall	[91]

Table 4.4: Process parameters found in literature that we will review and initially use in our experimental work, with P is the pressure in the chamber, T is temperature of the device, and t is the total heating time.

Chapter 5

Conclusions

In this report, we reviewed the state of the art in various lubricants that can be used at the microscale. Graphene is considered to be a promising material for the lubrication of MEMS devices with sliding surfaces. It is an attractive material with excellent mechanical and lubrication properties. Several graphene production methods were studied including the chemical vapor deposition (CVD) technique. With this method, we can deposit graphene directly on the MEMS sidewalls. This technique is suitable for large-scale applications, and it is flexible in terms of process conditions, that determine the graphene nucleation density and layer thickness.

The CVD method yields one to few layers of graphene. A high temperature activates the catalyst and facilitates the decomposition of the hydrocarbon gas into carbon and hydrogen atoms, the latter being removed by a hydrogen gas present during the reaction. Consequently, carbon atoms adsorb on the surface of the catalyst, and they diffuse into it. When cooling the catalyst, the carbon atoms precipitate out of the catalyst's surface and form graphene layers.

Since the CVD process is flexible, we can determine the suitable parameters for the direct synthesis of graphene on the MEMS sidewalls. Nickel is the structural layer in MEMS devices fabricated with MetalMUMPs, which is a micromachining process that uses electroplated nickel [93], which renders nickel the catalyst in this study. Methane and hydrogen will be used as the gases for the reaction. In addition, argon can be used to maintain a constant pressure for different gas mixture ratios between methane and hydrogen. The production of graphene will take place under atmospheric pressure. No pretreatment is required, which is usually a prerequisite to obtain monocrystalline graphene films. For the scope of this research, we don't need a specific type of graphene. Any type of graphene film that can lubricate is satisfactory for now.

Joule heating can generate high temperatures in order to activate the catalyst and decompose the methane gas. This enables us to deposit graphene locally by heating the parts of interest at low energy consumption. For the nickel catalyst, the deposition temperature is between 700 °C and 1000 °C, and the heating time should be between 30 s and 15 min in order allow sufficient carbon atoms to diffuse into the catalyst. The cooling rate is determined by the rate at which the heating power is reduced and by the heat capacity of the device. Since MEMS devices are very small, the heat capacity is very low; therefore, the cooling rate can be high. In order to further increase the cooling rate, a cooling gas can be introduced inside the process chamber.

One cannot compare flow ratios between a hot wall and a cold wall CVD process, because the kinetics and thermodynamics of the reactions are different. In literature, a hot-wall CVD is widely used, where the methane can already decompose in the gas phase and supply carbon to the surface. The gas-phase reactions in thermodynamic equilibrium and the thermo-catalytic reactions take place at the same time [114]. In a cold-wall CVD, however, only the substrate or a part of the substrate is heated, and the methane is not decomposed in gas phase. There is only thermo-catalytic decomposition of methane, since it decomposes on the surface of the substrate, and the carbon atoms diffuse inside the layer in the case of nickel [111]. Moreover, since heating takes place locally, only a small portion of methane will decompose; the one that is close to the heated part of the substrate. As a result, we have to take into account different process conditions in order to produce graphene on a MEMS structure.

The aim is to produce graphene on the rough sidewalls of the MEMS devices, the roughness of which influences the kinetics of the graphene growth process. The carbon mobility decreases if the sidewalls are rough, resulting in more carbon atoms being accumulated in certain locations. Furthermore, a rough surface is considered to have many defects, and these defects act as nucleation sites for graphene, similarly to grain boundaries and step sites of nickel [114, 111]. So, roughness is indeed a key parameter to take into account, as it influences the number of layers and the uniformity of graphene. Still, it is not a parameter we can vary in our experiments, as it is pre-defined by the fabrication process. In addition, every structure has a different surface roughness from another structure, which makes the reproducibility of graphene more challenging with regard to different MEMS sidewalls.

Surface roughness, as well as surface forces between contacting and sliding microscale surfaces, cause severe adhesion and friction issues in MEMS devices. Research has shown that graphene can reduce both adhesion and friction at the microscale [40]. However, no research has demonstrated how graphene can be applied as a lubricant in MEMS devices. This work illustrates that the local deposition of graphene is possible on microscale devices, using simple MEMS structures made of nickel. The direct synthesis of graphene can thus be applied to MEMS devices with contacting and sliding components. Once the issues concerning the MEMS lubrication are overcome, more exciting applications that involve MEMS with contacting and sliding structures will become commercially available in many industry applications.

Part II

Method

Chapter 6

Experimental setup

Our CVD system is, in fact, a cold-wall CVD system where only the substrate is heated. In our setup, Joule heating generates high temperatures up to around 1000 °C locally on the MEMS structures. A vacuum chamber connected to a probe station is used for our deposition experiments. A gas mixture of hydrogen and methane sets the pressure in the chamber to 1 bar. Figure 6.1 shows the experimental setup, and Appendix D includes detailed pictures of it.

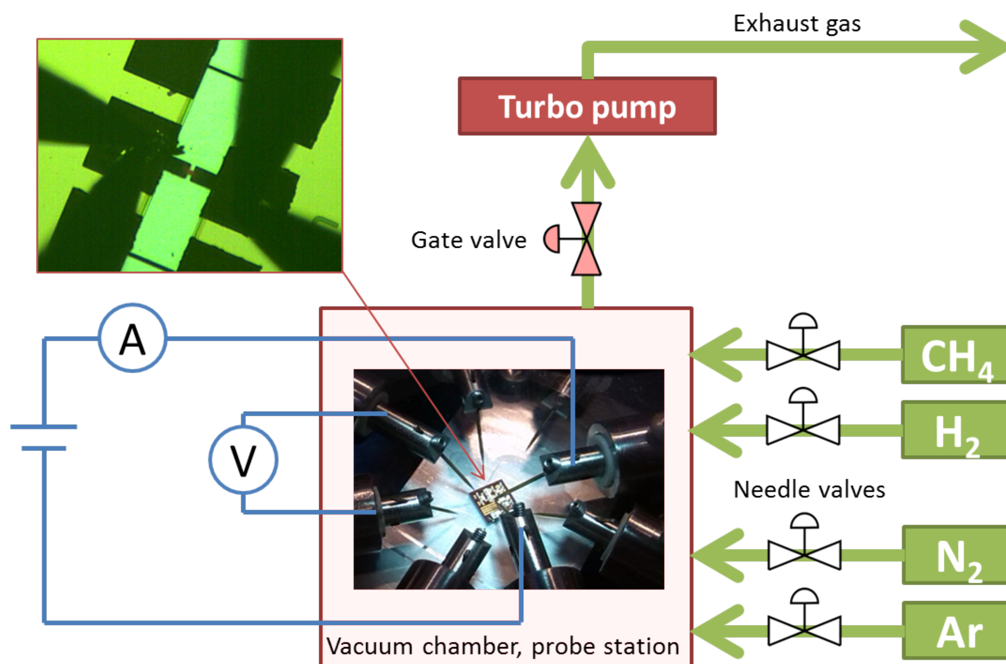

Figure 6.1: Schematic of the experimental setup that involves a vacuum chamber and the probe station (not shown in the figure), with a zoomed-in picture of four probes that make contact with the electric pads of the chip. The electrical circuit is indicated with blue lines, and the gas inlet and outlet are indicated with green lines.

A chip with MEMS structures is placed inside the vacuum chamber. The chamber can be sealed by tightening the bolts located around the perimeter of the probe station's viewport. It can be isolated from the vacuum pump by a gate valve. Gases can be introduced to the chamber by loosening needle valves that open and close the gas lines.

6.1 Pyrometer

In addition to our CVD system, we use an optical pyrometer, the Pyro MicroTherm by Pyrometer Instrument Company, to assess the local temperature of the MEMS structures subject to Joule heating. With an appropriate lens that can measure a size of 0.0127 mm, it is possible to investigate the temperature of structures with feature sizes of 6 µm and 8 µm.

A filament is situated in the viewport of the pyrometer. The filament is heated up to a certain temperature. A digital display unit is connected to the pyrometer and displays the temperature of the filament, and the temperature of the target. The emissivity coefficient of the material that is measured has to be set. The pyrometer compares the color emitted by the target with the one of the filament at a certain material-dependent emissivity value. The user compares the color of the glowing filament with the target, and adjusts the color of the heated filament until it disappears, as illustrated in the schematic drawings of Figure 6.2. A readout provides the temperature of the heated filament corrected with the emissivity value of the material of interest.

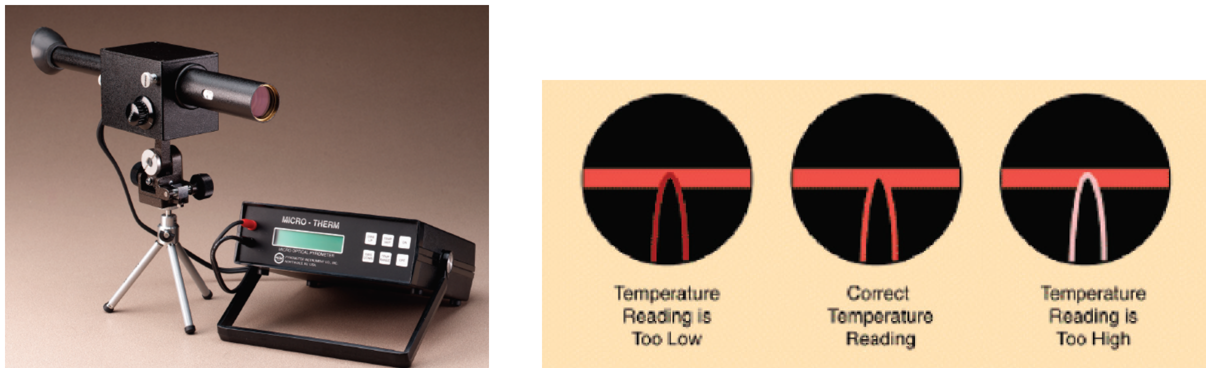

Figure 6.2: Picture of the Pyro MicroTherm optical pyrometer and schematic drawings during operation. The filament disappears when its temperature matches the temperature of the target, as seen in the middle drawing [121].

The accuracy of the pyrometer is ± 0.5%. Our eye is able to detect the emitted color with a precision of ± 1%. The temperature range of the filament that the pyrometer can display ranges from 700 °C to 3200 °C, and the emissivity value can be set between 0.01 and 1.0.

Emissivity

The emissivity coefficient of a material is the ratio of the energy that is radiated from the surface of the material divided by the energy that is radiated from a black body. This dimensionless number is an indication of the efficiency of the surface to emit thermal energy. Because every material has a different emissivity coefficient, every material emits a different amount of radiation at a certain temperature. Therefore, the temperature has to be corrected with the emissivity coefficient of the targeted material. Since the emissivity coefficient does not only depend on the type of material, but also on surface properties and temperature, we have to correct the filament temperature with the emissivity of electroplated nickel at around 1000 °C. In our calibration, we will use a value of 0.16 for electroplated nickel at 1093 °C [122].

6.2 Turbopump

The chamber is pumped down to vacuum before deposition to prevent residual gas molecules from reaching the MEMS structures, and to ensure that graphene does not get contaminated. We use the Pfeiffer HiPace 80 turbopump which is able to pump down our chamber to 10^{-8} mbar.

6.3 Probe station

The probe station is provided by McAllister and consists of eight probes. Those probe arms are vibration isolated in the chamber and can be accurately placed by translating them in x, y, and z direction. The chamber has optical access by a viewport. Detailed pictures of the probe station can be found in Appendix D.

6.4 Gases

During deposition, 500 mbar of methane and 500 mbar of hydrogen are used. 1 bar Argon may be used for a post-annealing treatment. The gases are supplied by Linde Gas Nederland, and their purities are given in Table 6.1.

Argon 5.0 instrument		Hydrogen 5.0 detector		Methane 5.5 scientific	
$\geq$ 99.999 vol%	Ar	$\geq$ 99.999 vol%	H_2	$\geq$ 99.9995 vol%	CH_4
$<$ 5 vpm	H_2O	$\leq$ 3 vpm	N_2	$\leq$ 5 vpm	O_2+N_2
$<$ 5 vpm	O_2	$\leq$ 5 vpm	H_2O	$\leq$ 1 vpm	C_xH_y
$<$ 0.2 vpm	C_xH_y	$\leq$ 2 vpm	O_2	$\leq$ 1 vpm	H_2O
		$\leq$ 0.5 vpm	C_xH_y		

Table 6.1: The quality of Linde Argon 5.0 instrument gas, Linde Hydrogen 5.0 detector gas, and Linde Methane 5.5 scientific gas.

6.5 Electrical circuit

For the temperature to rise locally on the MEMS structures due to Joule heating, we use a simple electrical circuit with a power supply connected in series with one ammeter and in parallel with one voltmeter. The resistance of the cables of the circuit is relatively high compared to the one of the bridges. Therefore, we use a four-point probe to measure accurately the voltage across each bridge. A diagram of the electrical circuit is given in Figure 6.3.

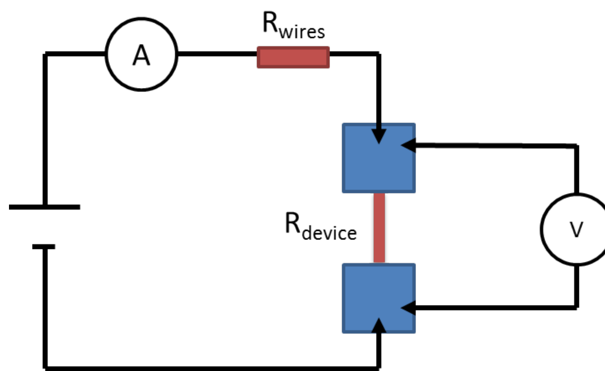

Figure 6.3: The circuit diagram used in our experiments. The resistances of the cables and the MEMS structure are indicated with red.

In most of our experiments, we use a direct current (DC) power supply, but we also use an alternating current one. In the latter, we use a switch to manually change the polarity and generate an AC source. The diagram of this circuit is shown in Figure 6.4.

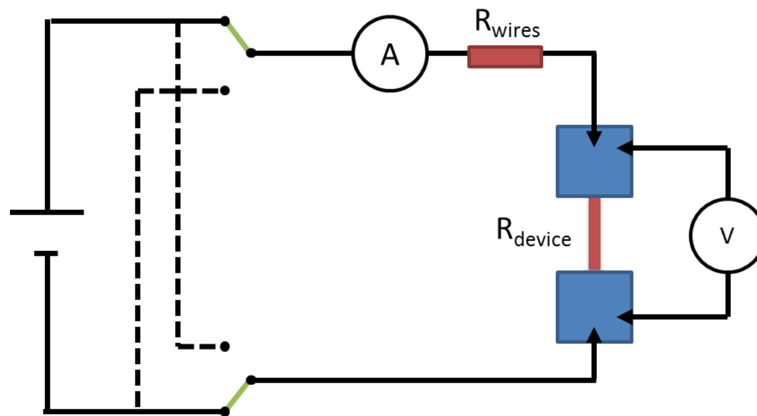

Figure 6.4: The circuit diagram with alternating current (AC) power supply. With a switch (indicated with green), the electron path follows the dashed lines, and the polarity changes. The resistances of the cables and the MEMS structure are indicated with red.

Chapter 7

MEMS structures

The MEMS structures of this study are made with a multi-user fabrication process from MEMSCAP, and, in particular, the MetalMUMPS, which uses electroplated nickel as the structural layer. The mask designs of the dies that we use in the experiments can be found in Appendix A.

7.1 Fabrication process

The MetalMUMPs process is described in the corresponding design handbook [123]. It consists of a 20 µm thick electroplated nickel layer, an approximately 2 µm thick gold layer, two nitride layers with a total thickness of 0.35 µm, and an isolation oxide layer; everything deposited on a silicon substrate. The process concludes with the formation of 25 µm deep trenches underneath the structures, so that they are completely suspended.

7.2 Structure design

For our experiments, we have designed MEMS structures that we will hereafter call 'bridges'. Such a bridge consists of a suspended beam with a smaller width in the middle part, and it is connected to two bond pads. We will use structures that have a width of 6 µm and 8 µm in the middle part. A scanning electron microscope (SEM) image is shown in Figure 7.1.

7.3 Nickel layer

Nickel will be used as the catalyst in the chemical vapor deposition (CVD) process, and it is the structural layer of our bridges. The thickness of MetalMUMPs structures can vary up to 20 ± 3 µm, which can result in large discrepancies between nickel layers of different MEMS bridges.

Since the electroplated nickel is polycrystalline, it has a lot of grain boundaries and thus a high surface roughness. These grain boundaries are favorable sites for graphene nucleation, due to high surface energy. For this reason, these areas have more atomic dangling bonds, attracting carbon atoms to the catalysts surface [124, 85]. The high surface energy at the grain boundaries helps in the methane decomposing into carbon and hydrogen atoms. Therefore, graphene will not grow uniformly on the polycrystalline nickel surface, and multiple graphene layers may be deposited on the grain boundaries. In addition, the graphene layers of several neighboring nucleation sites may overlap, yielding graphene layers with an even higher thickness. Impurities on the nickel surface can act as multiple nucleation sites too. An SEM image of the top of an 8 µm thick bridge covered with graphene is shown in Figure 7.2.

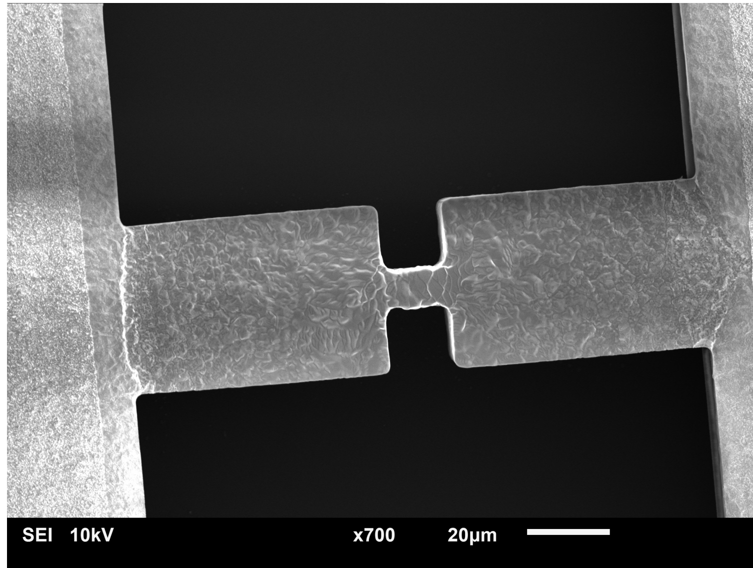

Figure 7.1: SEM image of a bridge with a width of 8 µm in the middle part. The left and the right side of the bridge is connected to bond pads (not shown in this figure).

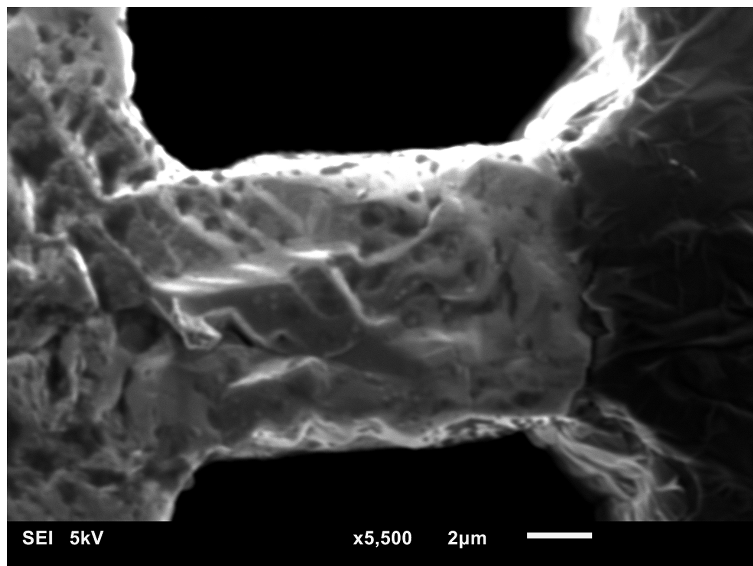

Figure 7.2: SEM image of the top of a bridge structure covered with graphene with a width of 8 µm in the middle part. The grains compose a rather rough surface.

Chapter 8

Experiments

8.1 Procedure

To perform our chemical vapor deposition (CVD) experiments, we first place the die with the MEMS bridges inside the vacuum probe station. Subsequently, the chamber is sealed and pumped down to vacuum conditions. When the pressure of the chamber is at 10^{-8} mbar, the chamber is separated from the turbopump by a gate valve. Hydrogen and methane are introduced to the chamber by unloosening the needle valves connected to the gas lines. The gases are introduced to the chamber until the latter reaches a pressure of 1 bar. The ratio of the partial pressures of methane and hydrogen is determined to 1:1. The probes then make contact with the pads of the structure to be heated with an external power supply. When a potential difference is applied to the structure, it dissipates heat, and the local temperature increases to 1000 °C. We use the pyrometer to determine the temperature accurately. The structure remains at this high temperature for an amount of time, which we will henceforward call the heating time. Afterwards, the electrical power is cut off or gradually reduced to zero, and the structure cools down to room temperature. The temperature as a function of time is plotted in Figure 8.1. Afterwards, we repeat the same procedure with another MEMS bridge. To remove the die with the bridges from the chamber, the probes are removed from the pads, the gate valve is opened, and the gases are led to the exhaust line. Then, the vacuum pump is switched off, and the chamber is vented with nitrogen to increase the pressure of the chamber to 1 bar. Then, we open the chamber, and we remove the die. This procedure has the advantage of fast cooling time with respect to a conventional CVD process. In addition, because the temperature rises locally through Joule heating, there is much less power consumption, since it is not needed to heat a whole oven, as in the case of a traditional CVD method.

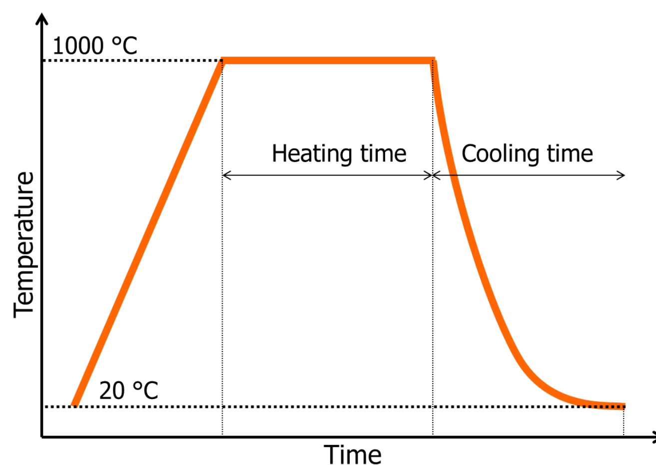

Figure 8.1: Temperature of a MEMS structure during the deposition experiments as a function of time. The gas mixture of methane and hydrogen is present throughout the whole heating and cooling process.

8.2 Variables

In our experiments, we use a heating time of 1 and 2 min. During this time, carbon atoms that emerged from the decomposition of methane diffuse into the nickel layer. At the same time, the grains of nickel increase in size. We use temperatures between 950°C and 1200°C for our different deposition experiments. Also, the cooling time plays a key role in the proper segregation of carbon from nickel, and the precipitation out if its surface. For this, we vary the cooling times by either cutting off the electrical power or by gradually decreasing it to zero fast or slowly in 0.5 s to 11 s. Post annealing under an inert-gas atmosphere, such as argon, can improve the structure of the as-grown graphene. This step was performed for 1 min and for the same temperature as during the deposition process.

8.3 Graphene characterization

Micro-Raman spectroscopy is a technique that provides us information on molecular vibrations, phonons, and other excitations in a crystal lattice that are unique in every material composition. It can be used to determine whether graphene layers have been deposited on the MEMS structures, and how many. We map both the top and sidewalls of our bridges. While accessing the top of any structure is quite straightforward, the die is placed on a 45° sample holder to access the sidewalls. The laser, used for the observation of the lattice vibrations, is focused on the middle part of the bridge, which we break into 15 measurement points. In chapter 9, we will elaborate further on the instrument's working principle and the assessment of graphene layers through the Raman response.

All the spectra were acquired with the Horiba LabRAM Scientific Micro Raman spectroscope. We used the tunable MELLES GRIOT 35 Lap 431 Argon-ion laser with a wavelength of 514.5 nm, an excitation energy of 2.41 eV, a power of 130 mW, and a spot size of 0.5 µm. Furthermore, a hole size of 1000 µm, a slit of 1000 µm, an acquisition time of 2 s, and an accumulation of 3 times were used in all the characterizations.

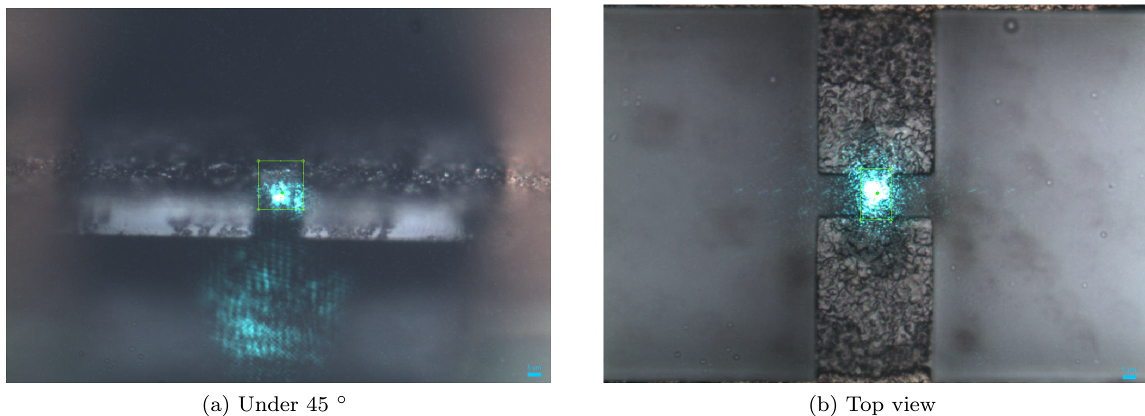

(a) Under 45 °

(b) Top view

Figure 8.2: Optical images during the acquisition with micro-Raman spectroscopy at the sidewall and top of a MEMS bridge. The laser spot is focused on the middle part of the MEMS bridge.

Chapter 9

Micro-Raman spectroscopy

Micro-Raman spectroscopy is a technique that provide us with information on the number of graphene layers, the crystal structure, and possible defects on the structure by observing molecular vibrations, phonons, and other excitations.

9.1 Working principle

A laser beam with a certain frequency is focused on a MEMS bridge. The laser light scatters, and the inelastic scattered light is collected, detected, and analyzed. Inelastic scattering causes the energy of the detected photon to be different from the energy of the incident photon (Figure 9.1).

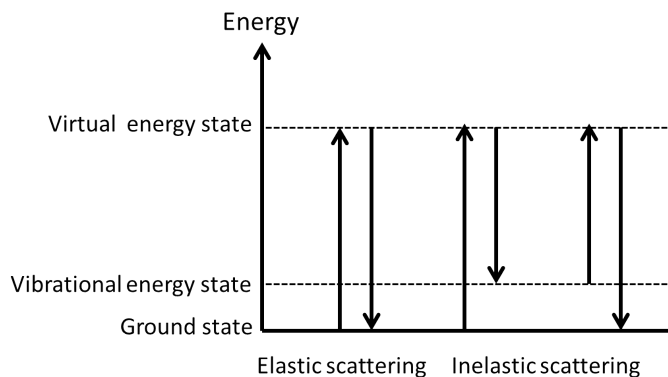

Figure 9.1: Schematic of the energy states in micro-Raman spectroscopy and the two ways in which scattering of photons is realized.

The photon of the laser interacts with the bonds of the probed molecule. The molecule is then excited to a virtual energy state. At the virtual energy state, the electrons have a forced oscillation and the energy does not remain constant. When the molecule goes to a lower vibrational energy state, it releases a photon. When the photon scatters inelastically there is a difference in energy between the scattered photon and the incident photon. This difference is called the "Raman shift", and it is expressed in cm^{-1}. In the Raman spectrum, high intensity corresponds to a high degree of vibrational rotations. The Raman shift Δw can be calculated from the energy E with equations (9.1), (9.2), and (9.3). The peaks in the Raman spectrum correspond to the phonon modes of the material [114], so that the Raman response can be used as means of material identification and verification.

$$E = hf \tag{9.1}$$

$$f = \frac{v}{\lambda} \tag{9.2}$$

$$\Delta w = (\frac{1}{\lambda_0} - \frac{1}{\lambda_0}) \tag{9.3}$$

9.2 Characterization of graphene

We can identify graphene and characterize the material properties by looking at the peak positions, the peak shapes, and the relative intensities of the peaks in the Raman spectrum. In graphene, two peaks appear at specific frequencies, and they are called the G peak and the 2D peak. In some cases, we can also observe the D peak.

The letter D of the D peak stands for defect or disorder. This peak is related to the defects in the crystal structure of graphene. For defected graphene, we find this peak at around $1350\,\mathrm{cm}^{-1}$. The position of this peak shifts with a change in the excitation energy [125]. The intensity is higher when there are more defects present, like dislocations, vacancies, and impurities. The D peak is present due to the in plane radial stretching of the carbon rings (Figure 9.2a).

The letter G of the G peak stands for graphite. This peak is present in the Raman spectrum of every graphitic material that contains sp^2 bonds [125]. We can observe this peak at around $1580\,\mathrm{cm}^{-1}$. The position of this peak hardly shifts with a change in the excitation energy. The peak position and intensity are influenced by doping, temperature, and number of layers, and the peak splits while straining graphene. The existence of the peak is evidence of in plane stretching of sp^2 bonded carbon atoms, see Figure 9.2b.

The 2D peak has twice the frequency of the D peak. We can find this peak at around $2700\,\mathrm{cm}^{-1}$ when there are well-ordered sp^2 bonds. It is an overtone of the D peak, and it does not depend on the G peak. The position and intensity of this peak is influenced by doping, strain, and excitation energy, but not by defects on the crystal structure. The peak emerges when two phonons with equal and opposite momenta are created. Similarly to the D peak, the 2D peak is also triggered by in plane breathing of the carbon rings (Figure 9.2a). The shape of the peak and the position depends on the number and the type of stacking between graphene layers; it also depends on temperature [125].

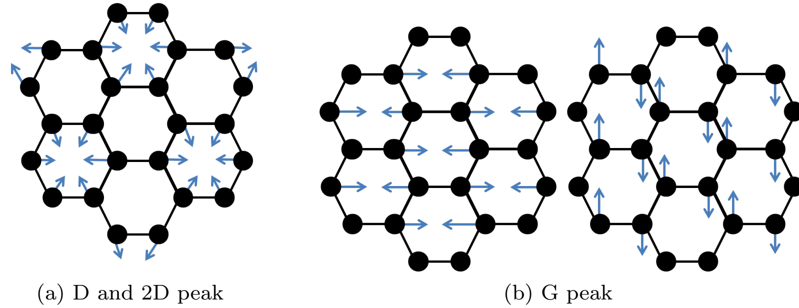

(a) D and 2D peak (b) G peak

Figure 9.2: Schematics of possible the phonon vibrations modes that give rise to the peaks seen in Raman spectra

9.2.1 Deviation in the Raman spectra

A lot of variables influence the Raman spectra, like strain, temperature, defects, impurities, and number of graphene layers. The width of the 2D peak changes when defects and wrinkles are present, as well as with increasing number of layers and polarization of the laser light. The intensity ratio between the G and 2D peaks can depend on the method with which graphene samples were prepared[126]. In addition, the type of substrate below graphene influences the Raman response due to the interaction between them. For instance, monolayer graphene on a nickel substrate will have a suppressed Raman signal, because nickel and graphene have a strong interaction [127]. The laser excitation energy influences the position of the peaks, their shapes, and their widths. Moreover, a high-power laser can heat up the substrate; in the case of nickel, a thermal conductivity of $90\,\mathrm{W/mK}$ means that it conducts the laser heat faster than SiO_2 (with a thermal conductivity of $1.5\,\mathrm{W/mK}$) by a factor of 100 [128]. This has to be taken into account when investigation Raman spectra of graphene, as most of the reported work in literature uses the spectra acquired by graphene on SiO_2 [129].

Furthermore, the way in which graphene layers are stacked can have an influence on the Raman response. In figure 9.3, we show the two types of stacking in a graphene structure: the AB-stacking (regular) and the turbostratic stacking (irregular or rotated) structure. A turbostratic structure causes weak interaction between the layers; therefore, the ratio of intensities between the 2D peak and the G peak can increase, depending on the degree of layer rotation. In turbostratic structures, the high-intensity 2D-peak does not depend on the number of layers; however, the peak position and width does depend on the number of layers [130, 131, 132]. For multiple graphene layers, the asymmetry of the 2D peak indicates AB-stacking, while a symmetric 2D peak indicates a rotated stacking [133]. The shape and height of the Raman peaks may even resemble the ones seen in the footprint of monolayer graphene [134]. Thus, the number of graphene layers can only be safely assessed through the intensity ratio and peak shape for structures that are regularly stacked [110]. Still, AB stacking is the most energetically favorable stacking for graphene, as long as there is sufficient energy for the carbon atoms to be arranged in such a configuration on top of the nickel surface [135, 110].

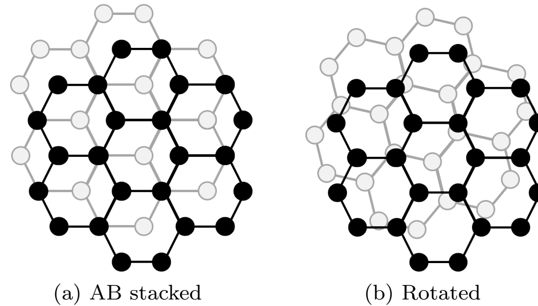

(a) AB stacked (b) Rotated

Figure 9.3: Schematics of the different types of stacking between graphene layers

9.2.2 Number of layers

Investigating the G and 2D peak in Raman spectra can help in determining the number of graphene layers. In particular, with an increasing number of layers, the 2D peak changes in shape, width, and position, while the G peak is seen to down-shift [136]. The intensity ratio between the 2D and the G peaks changes too. For monolayer graphene, the ratio I_{2D}/I_G is greater than or equal to 2 [137]. For bilayer graphene, the ratio is around 1. For few-layer graphene (FLG) of 3 to 5 layers, the intensity ratio is around 0.4. For few-layer graphene of more than 5 layers, the Raman spectrum resembles the one of bulk graphite [138]. The intensity ratio for graphite is the same as for few-layer graphene, but the shape of the 2D peak is asymmetric (Figure 9.4). The full width at half maximum (FWHM) is the width of the peak at half the maximum amplitude. At an increasing number of layers, and independently from stacking, the width of the 2D peak increases. The FWHM of the 2D peak of monolayer graphene is around 25–45 cm^{-1}, the one of bilayer graphene is around 45–60 cm^{-1}, and, finally, the one of few-layer graphene is around 70–90 cm^{-1} [85, 118, 138, 139, 140].

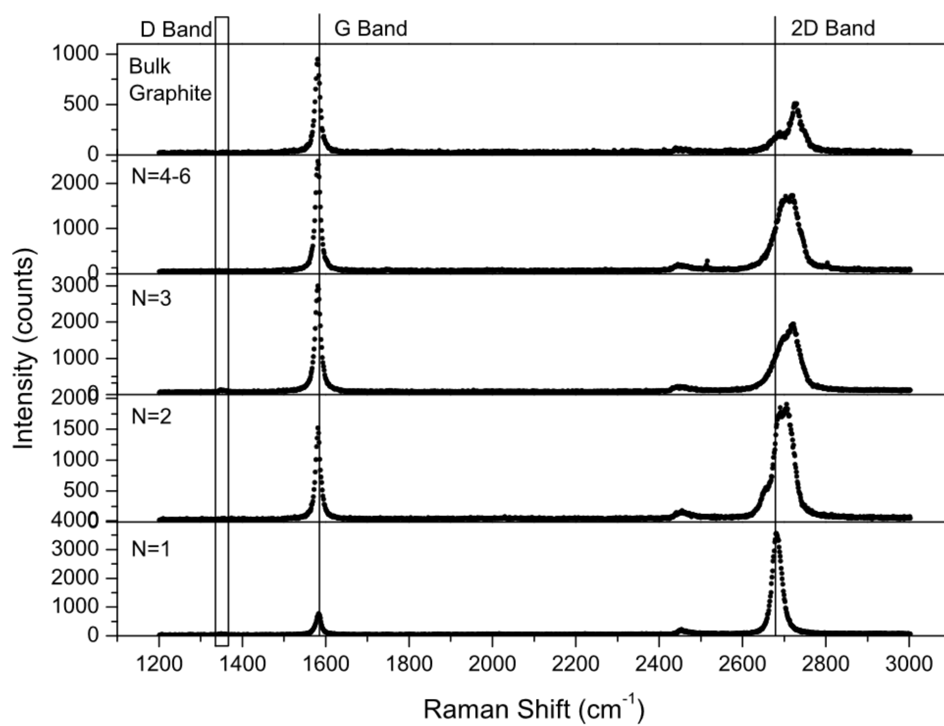

Figure 9.4: Raman spectra of bulk graphite, monolayer, bilayer, three-layer, and few-layer graphene measured with a laser at 514 nm on a SiO_2 substrate. N indicates the number of layers [141].

Part III

Results

Chapter 10

Experimental results

10.1 Graphene coverage on nickel structures

We carried out several deposition experiments with varying parameters to study what influences the growth of graphene on top and on the sidewalls of our MEMS bridges. We used micro-Raman spectroscopy to assess the number of layers and the graphene quality by probing 15 locations at the middle part of each structure. Such an experiment is carried out with structure C.5, which is shown in Figure 10.1. For clarity, we use a color code to indicate the number of graphene layers per location in the schematic images that illustrate our bridges. The Raman response of monolayer (a), bilayer (b), and few-layer graphene (c) of specific probed locations of structure C.5 is given in Figure 10.2. The spectrum of Figure 10.2a has an intensity ratio of about 2 and a FWHM of the 2D peak of around 45, indicating monolayer graphene. In Figure 10.2b, the intensity ratio is about 1.1, while the FWHM of the 2D peak is around 60, which is illustrative for bilayer graphene. Finally, the spectrum of Figure 10.2c has an intensity ratio of about 0.41 and a FWHM of the 2D peak of around 80. In addition, the intensity of the 2D peak is as low as the one of bulk graphite, when compared to the intensity of the G peak, but the shape does not match. All three observations together are indicative of few-layer graphene with a thickness of three to five layers. The Raman spectra that we acquired from other structures resemble the spectra seen in Figure 10.2. Furthermore, in Appendix B, the reader can find the combined spectra from the probed locations of structure C.5. The total coverage of all the structures with monolayer graphene, bilayer graphene, or few-layer graphene resulting from the probing of 15 locations on the top and on one sidewall can be found in Appendix C, together with the experimental growth conditions.

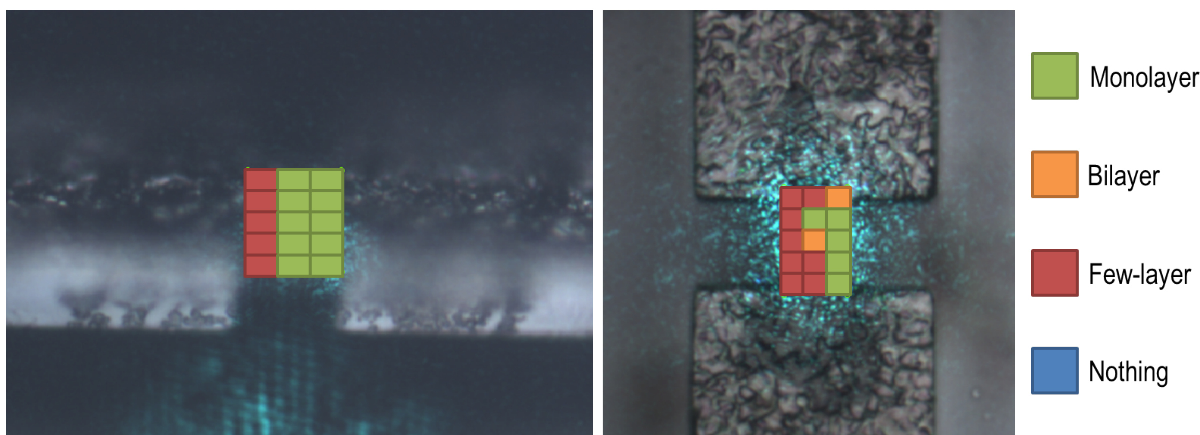

Figure 10.1: Optical images during the acquisition with micro-Raman spectroscopy at the top and at the sidewall of structure C.5. The laser spot is focused on the middle part of the bridge. The schematic indicates the number of graphene layers measured with micro-Raman spectroscopy.

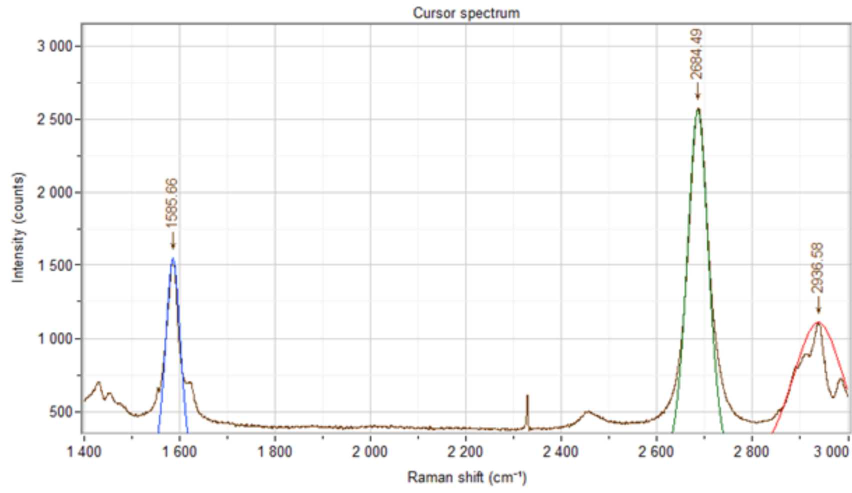

(a) Monolayer graphene

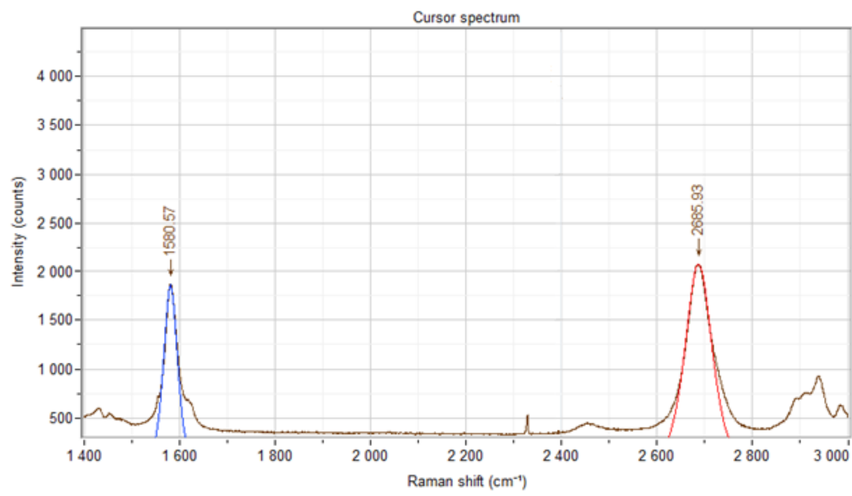

(b) Bilayer graphene

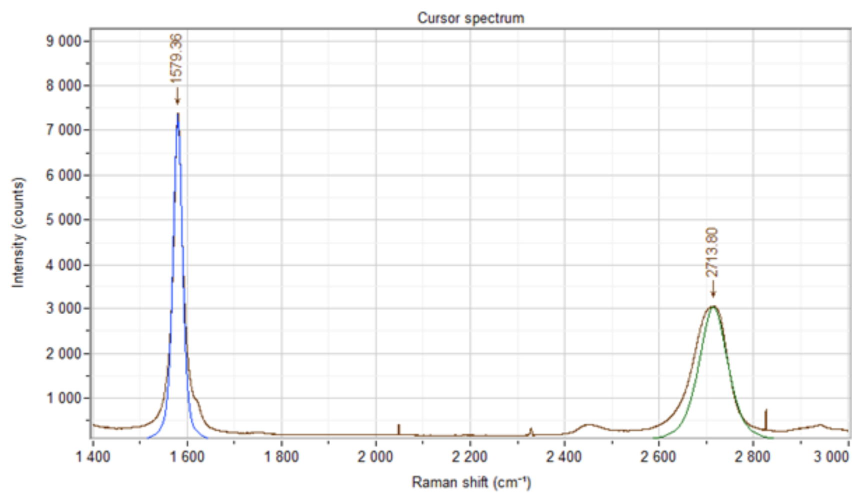

(c) Few-layer graphene

Figure 10.2: Raman spectra of monolayer (a), bilayer (b), and few-layer graphene (c) acquired from the sidewall of structure C.5.

An overview of the most representative experiments is shown in Figures 10.3, 10.4, and 10.5. In Figure 10.3, we investigate the spectra from structures B2.1, B2.4, and B2.7. These three structures have the same bridge width (8 µm), and they are all from die B2. During deposition, they had the same temperature of around 1085 °C for 2 min, but the cooling rate was different, as the structures cooled down in 5 s, 2 s, and 10 s respectively. In Figure 10.4, we assess the number of layers of four bridges that are from the same die. Two of them have the same width (8 µm), and, during depositing, they had the same temperature (about 1050 °C) and same cooling time (0.5 s). We set the heating time to 1 min for structure BNG.10, and 2 min for structure BNG.2. We varied the heating time also for the 6 µm wide bridges BNG.4 and BNG.12, to 2 min and 1 min, respectively. The temperature was set to about 1000 °C, and the structures cooled down in 0.5 s. Finally, Figure 10.5 shows the thickness of the graphene grown on structures A.6, C.5, BNG.8, A2.8, and A3.6. All bridges are 6 µm wide, but they are all from different dies. During deposition, they had a temperature between 1070 °C and 1200 °C for 2 min, and they all cooled down in 0.5 s. These experiments are meant to assess the reproducibility of the as-grown graphene on structures that come from different wafers of the MetalMUMPs process.

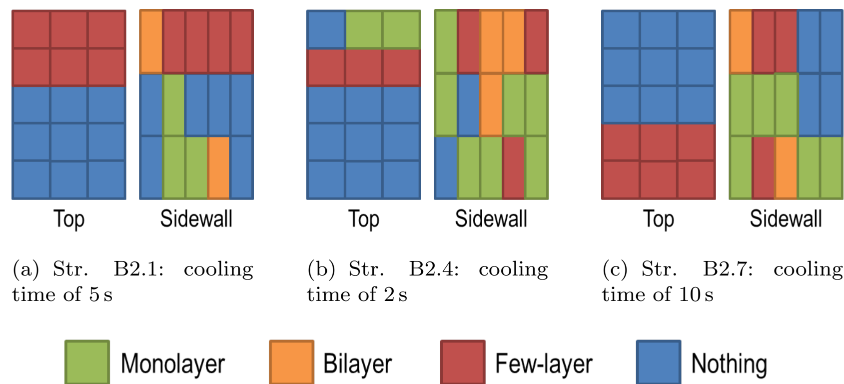

(a) Str. B2.1: cooling time of 5 s

(b) Str. B2.4: cooling time of 2 s

(c) Str. B2.7: cooling time of 10 s

Figure 10.3: Schematics of the number of graphene layers on both the top and one sidewall for structures that cooled down in different times. All structures are on die B2. The structures have a bridge width of 8 µm and were heated at around 1085 °C for 2 minutes.

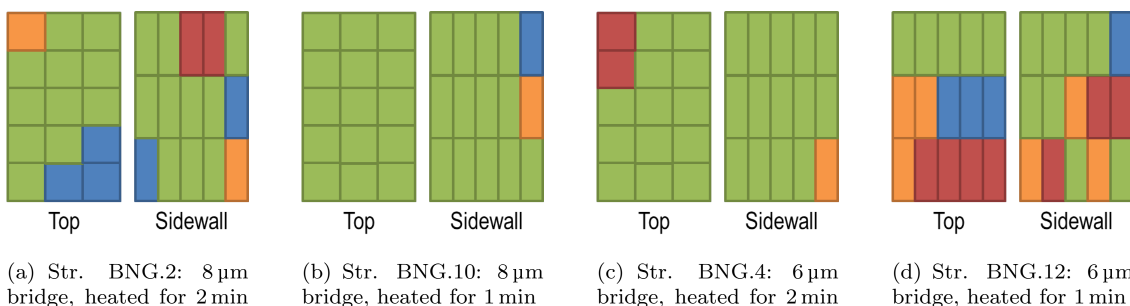

(a) Str. BNG.2: 8 µm bridge, heated for 2 min

(b) Str. BNG.10: 8 µm bridge, heated for 1 min

(c) Str. BNG.4: 6 µm bridge, heated for 2 min

(d) Str. BNG.12: 6 µm bridge, heated for 1 min

Figure 10.4: Schematics of the number of graphene layers on both the top and one sidewall of two structures with a bridge width of 6 µm, and two structures with a bridge width of 8 µm. All structures are on die BNG. The structures were heated at around 1000 °C for 1 min and 2 min, and they cooled down in 0.5 s.

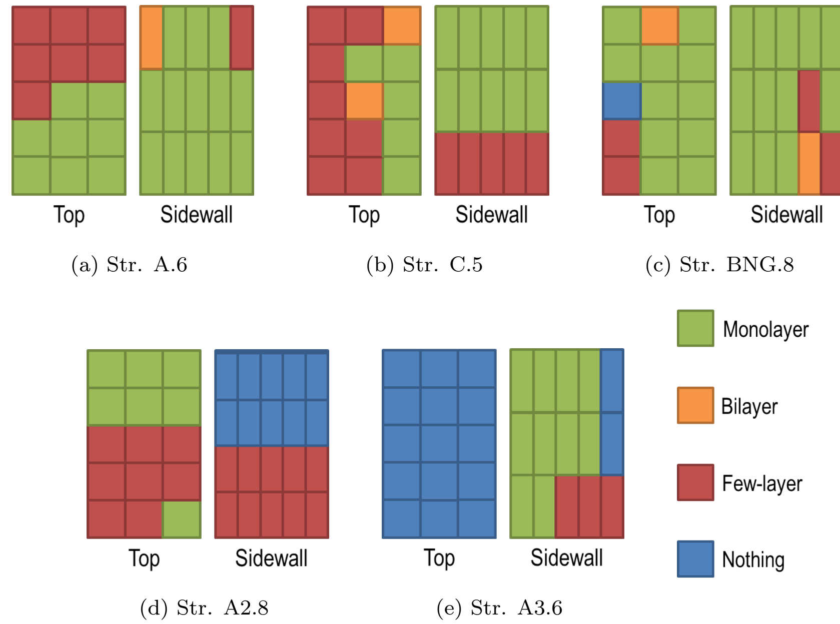

Figure 10.5: Schematics of the number of graphene layers on both the top and one sidewall of structures from different dies, and with a bridge width of 6 µm. The temperature of the structures was between 1070 °C and 1200 °C for 2 min, and they cooled down in 0.5 s.

10.2 Influence of temperature on coverage

We conducted deposition experiments on structures that are heated for two minutes at different temperatures. The temperature range was between 925 °C and 1205 °C. In Figure 10.6, we plot the total coverage of the structures with graphene layers, as a function of temperature. The different colors of the data points correspond to the different dies used, the structures of which had a bridge width of either 6 µm (diamond marker) or 8 µm (circle marker).

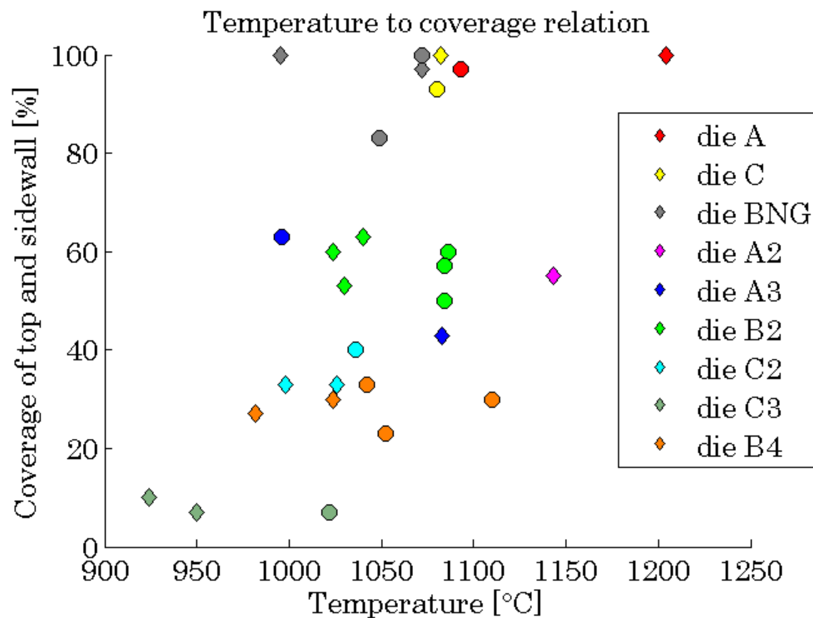

Figure 10.6: The total coverage of both the top and one sidewall of the structures with graphene layers, as a function of temperature. The experiments were conducted with both 6 µm (diamond marker) and 8 µm (circle marker) wide bridges that were heated for 2 min.

10.3 Influence of cooling time on coverage

The cooling time is very important for the precipitation of carbon atoms out of the nickel layers. for this reason, we investigate how the cooling time influences the coverage of the structures with graphene layers. In Figure 10.7, we show the results for structures with both 6 µm (diamond marker) and 8 µm (circle marker) wide bridges from different dies that were heated for 2 min between 1000 °C and 1100 °C, and they were cooled down in different times, from 0.5 s to 11 s.

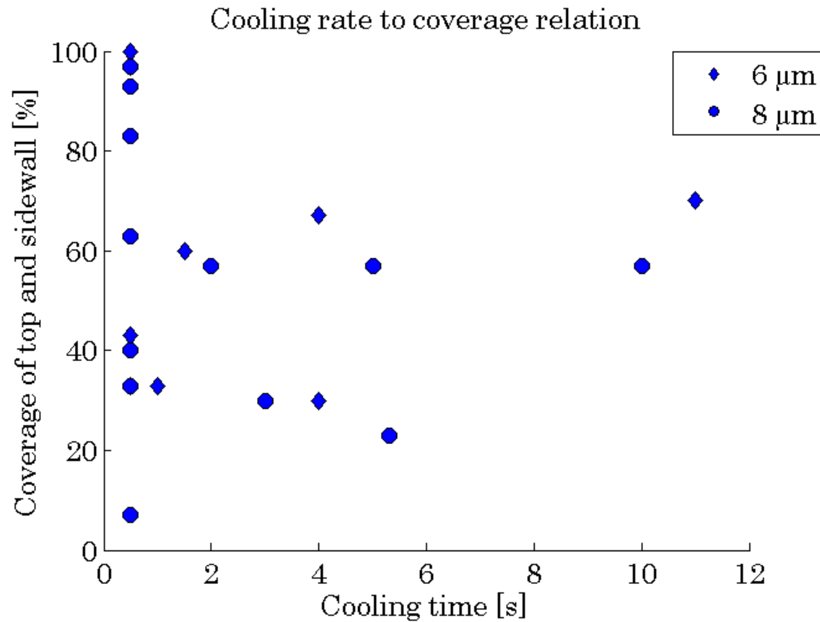

Figure 10.7: The total coverage of both the top and one sidewall of the structures with graphene layers, as a function of cooling time. The experiments were conducted with both 6 µm and 8 µm wide bridges that were heated for 2 min between 1000 °C and 1100 °C, and they cooled down in different times.

10.4 Influence of heating time on coverage

To evaluate the influence of heating time on coverage, we conducted experiments with 6 µm (diamond marker) and 8 µm (circle marker) wide bridges from different dies that were heated for 1 min and 2 min between 1000 °C and 1100 °C. The total coverage of both the top and one sidewall of such structures is illustrated in Figure 10.8.

10.5 Influence of post annealing on coverage

As discussed in Chapter 4, a post treatment of annealing can help in rearranging the graphene structure and, thus, in decreasing the number of defects. However, the deposited layers may decrease in number. We carried out this post treatment step with the structures of die BNG, to evaluate whether they can yield monolayer graphene with reduced defects. The structures were heated at temperatures between 1000 °C and 1080 °C, and the surrounding atmosphere was argon at 1 bar. The heating time was 1 min for all structures, and their cooling time was 0.5 s. Figure 10.9 compares the number of graphene layers of the structures before and after this post treatment step.

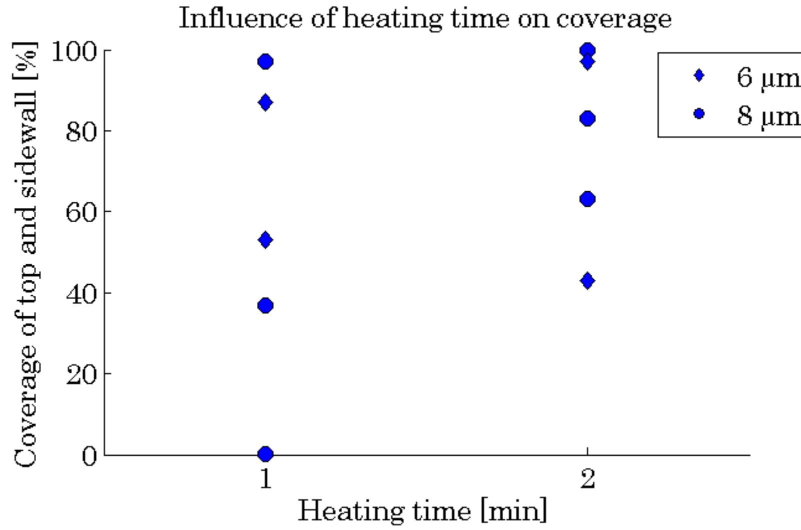

Figure 10.8: The total coverage of both the top and one sidewall of the structures with graphene layers, as a function of heating time. The experiments were conducted with both 6 µm and 8 µm wide bridges from dies A2, A3, and BNG. The bridges were heated between 1000 °C and 1080 °C, and they cooled down in 0.5 s.

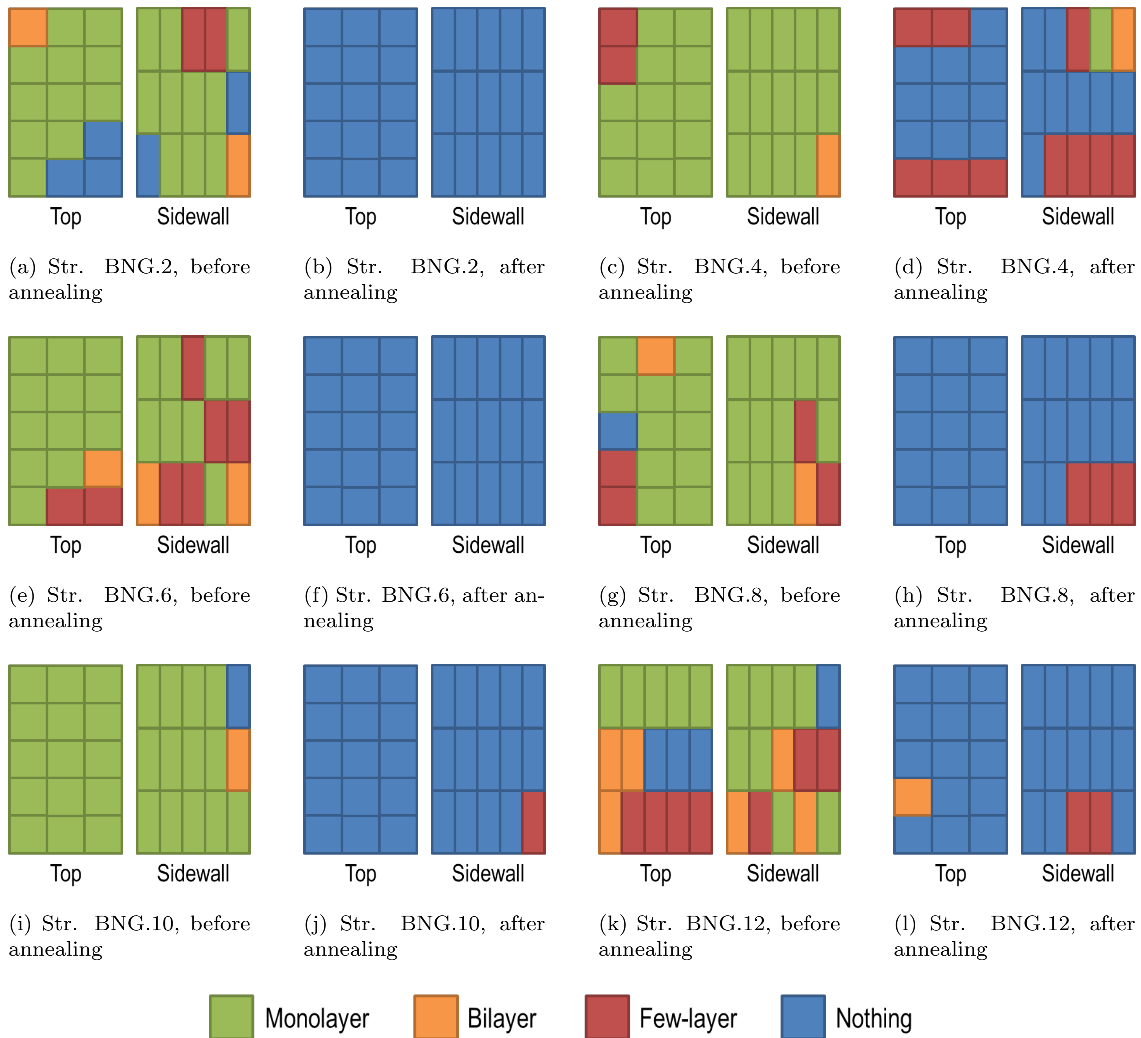

Figure 10.9: Schematics of the number of graphene layers of the top and one sidewall for six different structures of die BNG before and after an 1 min post treatment step at high temperature in argon.

10.6 Influence of alternating current on coverage

For structures of which the top is not completely covered, there is a preference for graphene to grow on one side of the bridge. In particular, Figure 10.10 indicates that there is a preference towards the negative pole of structures from dies B2, C2, and C3, where we can mostly find few-layer graphene. The growth conditions and bridge width of these structures can be found in Appendix C.

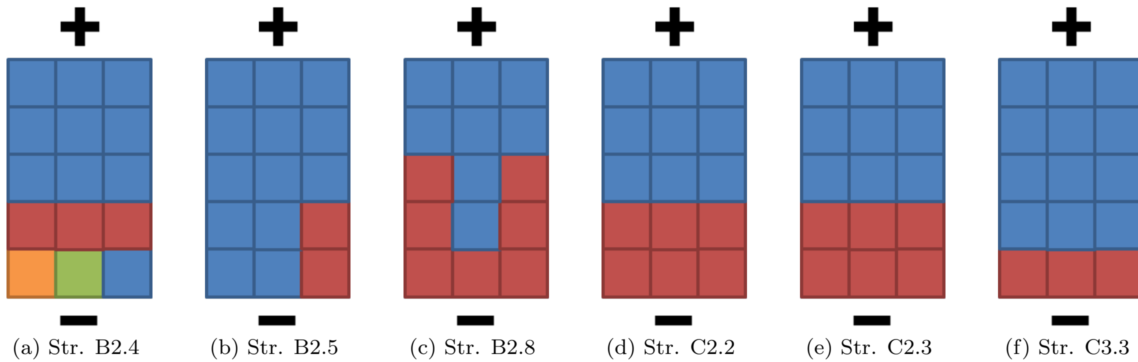

Figure 10.10: Schematics of the number of graphene layers of the top for structures from dies B2, C2, and C3. The plus sign indicates the positive electrical polarity, and the minus sign indicates the negative electrical polarity of the bridge.

Carbon appears to diffuse towards and accumulate at the negative pole of the MEMS bridges potentially due to negative polarity, and it may no longer show this preference when we use an alternating current (AC) source. We tested this hypothesis in structures from die A4 by manually changing their polarity with a switch to generate an AC source. The polarity of two structures (with a bridge width of 6 µm and 8 µm) was changing with a frequency of 0.03 Hz, while the frequency for the other two structures (also with a bridge width of 6 µm and 8 µm) was set to 1 Hz. During deposition, they had a temperature between 1000 °C and 1025 °C for 2 min, and they all cooled down in about 10 s. The result of these experiments is shown in Figure 10.11.

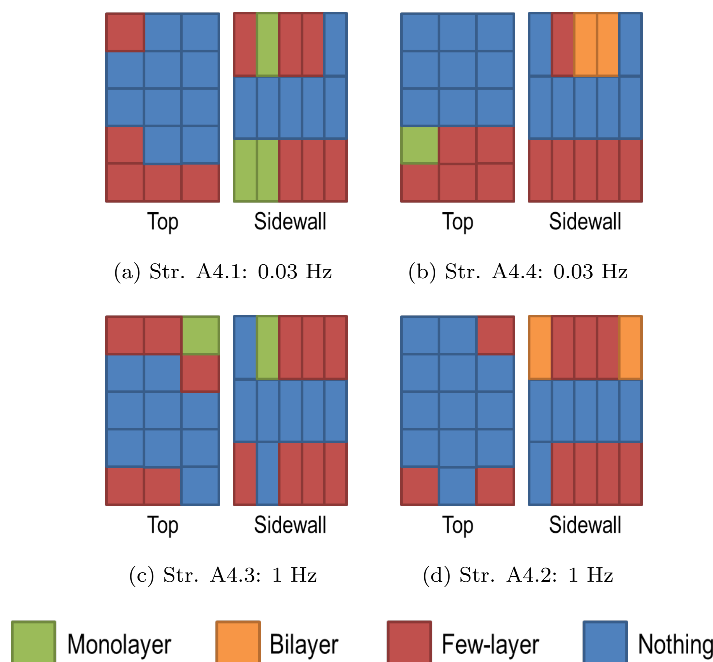

Figure 10.11: Schematics of the number of graphene layers of the top and one sidewall for structures from die A4. During deposition, the polarity was changing with a frequency of 0.03 Hz or 1 Hz.

Chapter 11

Discussion of the results

11.1 Die-dependent coverage

In Figure 10.6, we plotted the total coverage of both the top and one sidewall of structures with graphene layers, as a function of temperature. In this figure, we observe that three dies (A, C, and BNG) have structures with coverage of at least 80 %. Dies A2, A3, and B2 have structures that exhibited 40 % to 60 % coverage, while the 'least successful' structures were in dies C2, C3, and B4, with coverage of less than 40 %. In Appendix C, however, the reader can find out that the structures in A3 and B2 have sidewall coverage of about 85 %, whereas the top coverage was between 0 % and 40 %. Nevertheless, it appears that the type of die has a significant influence on coverage, while the structures belonging to the same die generally have about the same percentage of coverage. Therefore, the type of die seems to suppress experimental parameters, such as temperature, heating time, and cooling time. In particular, we cannot see an influence of either the temperature or the heating time on the coverage of the structures. Both 1 min and 2 min of heating can result in either a high or a low coverage with graphene layers. In addition, both heating at 1200 °C and heating at 1000 °C can result in an almost fully covered or a partially covered structure with graphene. Moreover, either extremely fast cooling or medium cooling can result in the same coverage of the structures.

The nickel structures that are fabricated on the same wafer will generally share the same properties, like layer thickness, resistivity, and crystallinity. Thus, some structures can 'behave' similarly under the same conditions during the deposition experiments, as long as they belong to the same die, or, to another die that comes from the same wafer. However, even for structures that come from the same wafer, it should not be taken for granted that they have the same roughness. This surface property depends on the orientation and size of grains, which, in turn, will determine which sites allow carbon to diffuse inwards (during heating), and outwards (during cooling). Consequently, the coverage with graphene layers is strongly affected by the roughness of the nickel layer. In most structures, mainly the sidewall was covered with graphene layers, which is presumably less rough compared to the top of the structures. A smoother surface can lead to more uniform graphene layers, if not to monolayer graphene with almost no defects, since the total length of grain boundaries is shorter compared to the one of a rougher surface. Another reason why it is mainly the sidewalls that have a better coverage is probably because they cool down faster than the top of the structures due to heat losses by convection. Still, this requires further investigation.

11.2 Post annealing

A post treatment step with annealing results in the removal of graphene layers in our experiments. The structures that are almost covered with graphene layers have hardly any graphene layers left after annealing in argon. This result is particularly remarkable, because argon is an inert gas, and it should not react with the carbon atoms on the nickel surface. As far as etching is concerned, and as we already mentioned in chapter 4, oxygen can remove carbon atoms at temperatures higher than 400 °C. In Table 6.1, we illustrated that hydrogen, methane, and argon, all in their gas form, contain oxygen. During the

chemical vapor deposition with hydrogen and methane, more graphene layers are grown than are etched due to the presence of oxygen. During post annealing, however, the gases responsible for the growth, namely methane and hydrogen, are no longer present. Consequently, graphene layers are probably etched at a much higher rate than carbon atoms are able to precipitate out of the nickel bulk to replenish the removed graphene layers. Therefore, the resulting structures will have no graphene layers, or they will only have small graphene patches on a few spots.

11.3 Electromigration

In some experiments, several structures turned out to be covered by graphene layers only on one side of the bridge. It appears that carbon has the tendency to diffuse towards the negative electrical polarity of the structure. By applying an alternating current during heating, the structures had graphene layers on both sides of their bridges after deposition. Still, no complete coverage was achieved.

Electromigration can be a plausible explanation why carbon atoms tend to move towards one side of the structure. In electromigration, ions are pushed towards one side by a so-called 'electron wind' and by an electrical field. In our case, the ions are the carbon atoms that donated or received electrons. In fact, carbon atoms, either ionized or neutral, are interstitial in the nickel lattice, and they can move fast through the nickel lattice. A measure of their velocity can be given by the current density, $J = I/A$. In our experiment, the current density is: $2 \times 10^6\ \mathrm{Am^{-2}}$, which is high enough to trigger electromigration. It is then probably due to electromigration that graphene layers are selectively deposited on one side of the structure, which can be either the one with the positive or with the negative electrical polarity. However, even with an alternating current during heating, the structures were not fully covered with graphene. It is then important to apply alternating current also during cooling. We argue that electromigration can play a role on the surface of the nickel instead of the bulk. It is also possible that the temperature gradient over the structure causes graphene to be deposited at one side of the structure, since only the middle part of the bridge is heated to a very high temperature. This temperature gradient can result in different diffusion rates. Therefore, carbon can accumulate at certain locations of the structure depending on the geometry. To conclude, it cannot yet be fully explained how carbon atoms diffuse towards one side of our nickel structures.

11.4 Limitations of micro-Raman spectroscopy

To assess the number of graphene layers, we probed 15 locations of the whole bridge with micro-Raman spectroscopy. The spot size of the laser is 0.5 µm, while the smallest bridge is 6 µm in width. Therefore, the distance between the measured spots is long enough to ensure that a single Raman response comes from a single probed location, and there is no overlap in the measurement points.

In chapter 9, we elaborated on possible variables that can influence the Raman response, which can introduce an uncertainty in the number of layers we assign to the different acquired spectra. To be sure, we need to investigate another method to determine the number of graphene layers, next to micro-Raman spectroscopy. One method involves isolating the graphene layers from the nickel structures by removing the latter with etching. The suspended graphene layers can be imaged by either a contrast method or atomic force microscopy (AFM). The combined result of the two methods can provide insights on the number of layers. However, if we follow this procedure, we would 'sacrifice' a whole die of nickel structures to isolate only the layers of graphene deposited on only one structure. Moreover, it is difficult to find such a small graphene flake in a solution after etching away the nickel structure. Another technique that can be used to characterize and assess the number of graphene layers is scanning tunneling microscopy (STM). The stacking order (AB stacking or turbostratic) of the graphene layers can be identified with this technique. However, the technique is effective in visualizing the first two graphene layers. STM, then, can only be used to determine how these two layers are stacked together, and the type of stacking is assumed to be the same throughout the remaining layers in few-layer graphene. As long as AB stacking is still energetically favorable, micro-Raman spectroscopy will assign the response of monolayer graphene correctly, thus, is still a reliable method for graphene characterization.

Part IV

Conclusions

Chapter 12

Conclusions and recommendations

In this work, we researched the possibility to deposit a lubrication material on MEMS structures. Literature has already shown that graphene can reduce adhesion and friction at the microscale, but the direct graphene synthesis on MEMS devices has not been demonstrated yet. In this report, we explored the possibility to grow graphene on MEMS sidewalls. Furthermore, we investigate the variables that influence the deposition of graphene. The contribution of this work can be exploited to develop MEMS devices with sliding structures that are less prone to friction-related failures.

12.1 Conclusions

In the literature study, we investigated the available lubrication materials for MEMS devices. For our experiments, we opted for graphene, due to its excellent mechanical and lubrication properties, the potential to replenish the layer, and the possibility to use it in both dry and humid air. Because of the size of the MEMS devices, a transfer of graphene layers to the MEMS surface can damage the device and the layers. Therefore, it was decided to deposit graphene directly on the MEMS surface. A comparison between the production techniques of graphene revealed that the chemical vapor deposition (CVD) method is the appropriate technique for depositing graphene layers locally on MEMS surfaces. Moreover, it was found to be the best candidate in terms of quality, costs, flexibility, and of its potential for large-scale applications.

The CVD method is flexible in terms of process conditions. In order to deposit one to a few layers of graphene on MEMS sidewalls, we determined the suitable process parameters. Nickel was used as the structural layer and catalyst for the reaction, and we generated high temperatures between 950 °C and 1200 °C locally through Joule heating. Methane was used as the carbon source for graphene deposition, and hydrogen was present during the reaction for the decomposition of methane into carbon atoms. In the deposition experiments, we heated MEMS structures with 6 µm and 8 µm wide bridges for 1 or 2 min, and we cooled them down in 0.5 s to 11 s. For some structures, a post treatment step with annealing was performed for 1 min under argon atmosphere at the same temperature as during deposition. We carried out our deposition experiments with a probe station compatible with the CVD process, and we assessed the number of layers and quality of graphene with micro-Raman spectroscopy.

Our experiments revealed that it is possible to deposit graphene locally on MEMS sidewalls by CVD. All deposition experiments resulted in MEMS bridges with at least a few spots of graphene layers. From micro-Raman spectroscopy, we found out that the coverage of the structures with graphene layers varied a lot between experiments. The key factor was the die itself; different dies seem to have structures that are different in terms of dimensions, roughness, and degree of contamination. Therefore, it was hard to reproduce the results on structures belonging to different dies, or, to be more precise, to different wafers. The experiments revealed that the temperature, heating time, and cooling time had little influence on the total coverage of the bridges with graphene layers. The effect of post annealing on the coverage was examined, and it was revealed that annealing under argon atmosphere removes graphene layers. From this result, it can be deduced that graphene layers were etched by oxygen residues in the argon gas. During the experiments, we observed that graphene layers are sometimes mainly deposited at the negative pole

of the structures. For this reason, we conducted some deposition experiments with an alternating current instead of a direct current. These experiments demonstrated that the direction of the current had an influence on the deposition of the graphene layers. However, more research is needed into this effect, as the structures were still partially covered with graphene.

In conclusion, we demonstrated the successful deposition of graphene on the top and sidewalls of MEMS structures. It is possible to grow monolayer graphene on microscale polycrystalline nickel structures, presumably due to the use of Joule heating and the advantage of an extremely fast cooling time, which is not possible at the moment with a conventional CVD system. The results of this report can be taken into account for further research into applying graphene as a lubricant on MEMS surfaces, and for the development of MEMS devices with sliding structures for reduced friction and wear.

12.2 Recommendations

Although successful, the direct deposition of graphene on MEMS structures is deemed to several improvements. For instance, once in contact with the bond pads of the die during the experiments, the probes move and scratch the structures when there is a gas flow in the chamber. Therefore, we had to first introduce the gases inside the chamber and then place the probes on the bond pads of the die. Because of this, we were not certain whether the ratio between methane and hydrogen remained at 1:1 throughout all deposition experiments on one single die, as every next methane decomposition would take place with the momentary ratio resulting from the preceded decomposition. By wire-bonding the die, we have the freedom to introduce and remove gases from the chamber, and any slight pressure change will have no effect on our structures.

We used a pyrometer to optically assess the temperature of our structures that requires an emissivity value. For this, we inserted an emissivity value found in literature. However, the emissivity is not only material and temperature dependent, but it is also influenced by surface properties. A setup of a heating stage combined with a pyrometer can be used to determine accurately the emissivity of the electroplated nickel used as the structural layer of our structures. Afterwards, this value can be used to calibrate the temperature of the structures prior to the deposition experiments.

It is recommended to automate the power that is supplied to the structures during the deposition experiments. At the moment, the heating time is set manually for the structures to reach high temperatures of around 1000 °C. Since reactions already take place from 700 °C, it is important that the time to heat up is the same in every experiment. The automation of supplying electrical power to our structures can also provide control on the cooling time.

As far as the alternating current experiments are concerned, it would be interesting to apply a power with a much higher frequency, like in the range of 10–1000 Hz. With a programmable AC power source, such experiments should be possible. In addition, more research is needed to study the influence of electrical polarity and current on carbon diffusion inside the MEMS structures and the diffusion mechanisms.

Future research efforts could involve minimizing disparities between dies from their production stage. Essentially, when we do not fabricate the dies with a multi-user process, but with a single-user one that follows a user-defined microfabrication procedure, the influence of the type of die on the coverage of the structures with graphene can be minimized. Then, the experimental variables like temperature, heating time, and cooling time can be fine-tuned to yield the desirable coverage.

One can look at the possibility to grow graphene on a nickel structure by doping it with carbon without any methane gas. When the structure is subsequently heated in an oven instead of by Joule heating, graphene layers can be deposited on any location of the structure. This will give some freedom in designing MEMS structures in a different way. Additionally, a nickel layer with dissolved carbon in it can be annealed once the graphene layer is worn off. Carbon atoms which are yet to segregate from the bulk and precipitate out of its surface can then replenish the damaged layer. Nevertheless, one should be careful not to have oxygen present during heating to prevent etching of graphene.

An interesting outlook would be to conduct deposition experiments on sliding MEMS sidewalls. The coefficient of friction of devices covered with graphene can then be compared with the one of devices without any graphene. Consequently, research can reveal the optimum number of graphene layers that will allow MEMS surfaces to slide with the lowest possible coefficient of friction.

Part V

Appendix

Appendix A

Mask designs of the dies

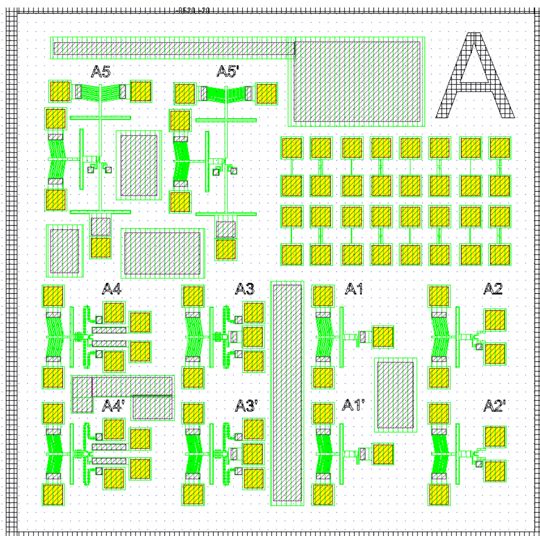

(a) Die A, A2, A3, and A4

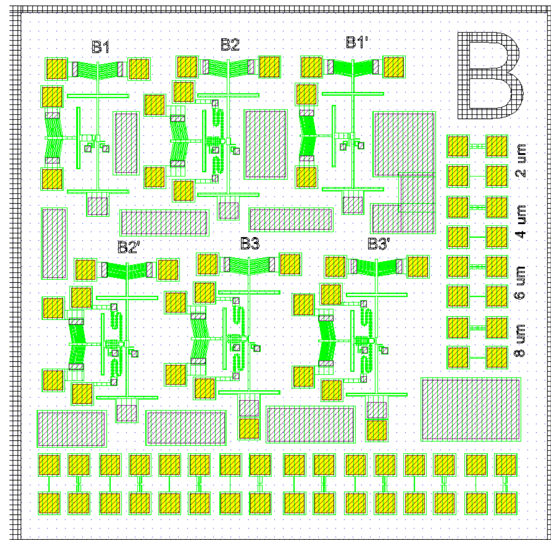

(b) Die B2, B4, and BNG

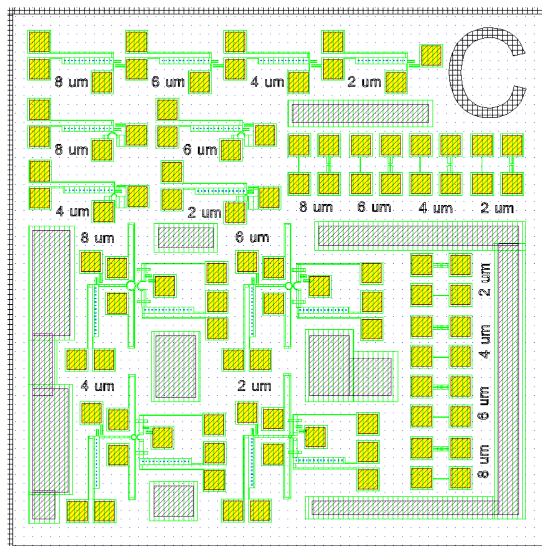

(c) Die C, C2, and C3

Figure A.1: Mask designs of the dies that are used in the experiments. Only the 6 and 8µm bridges are used in the experiments.

Appendix B

Raman response of structure C.5

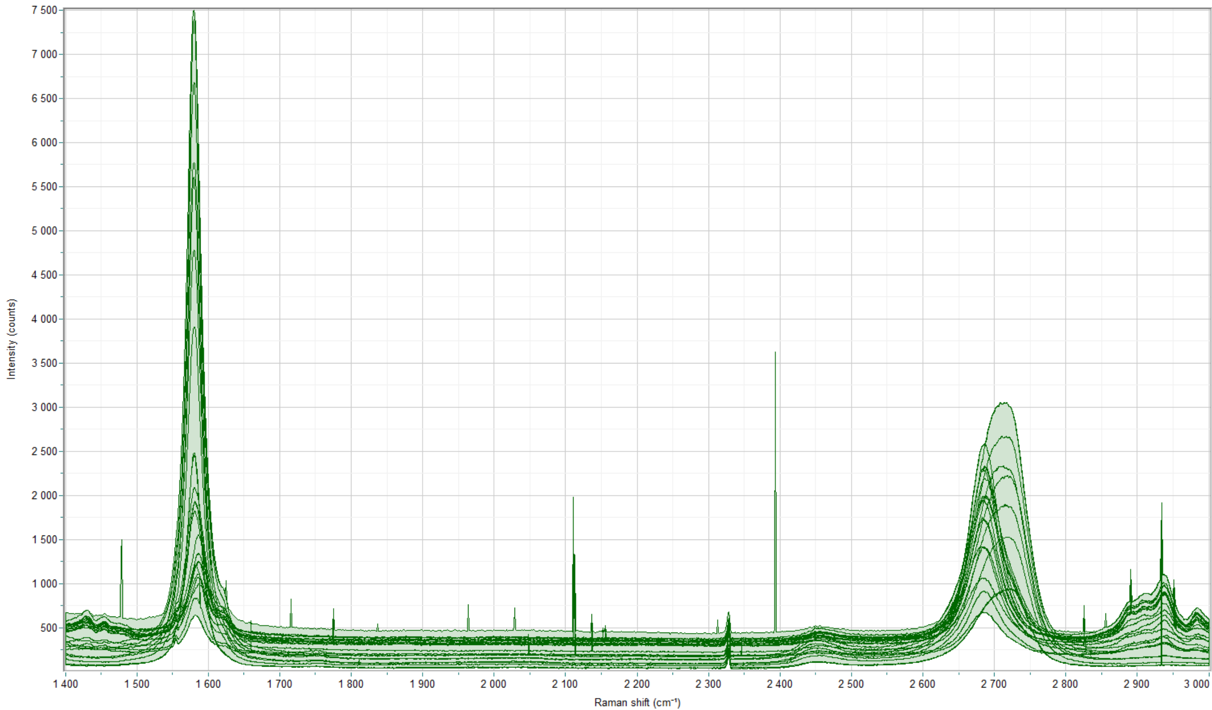

Figure B.1: The total Raman spectra of the sidewall of structure C.5, resulting from the probing of 15 locations.

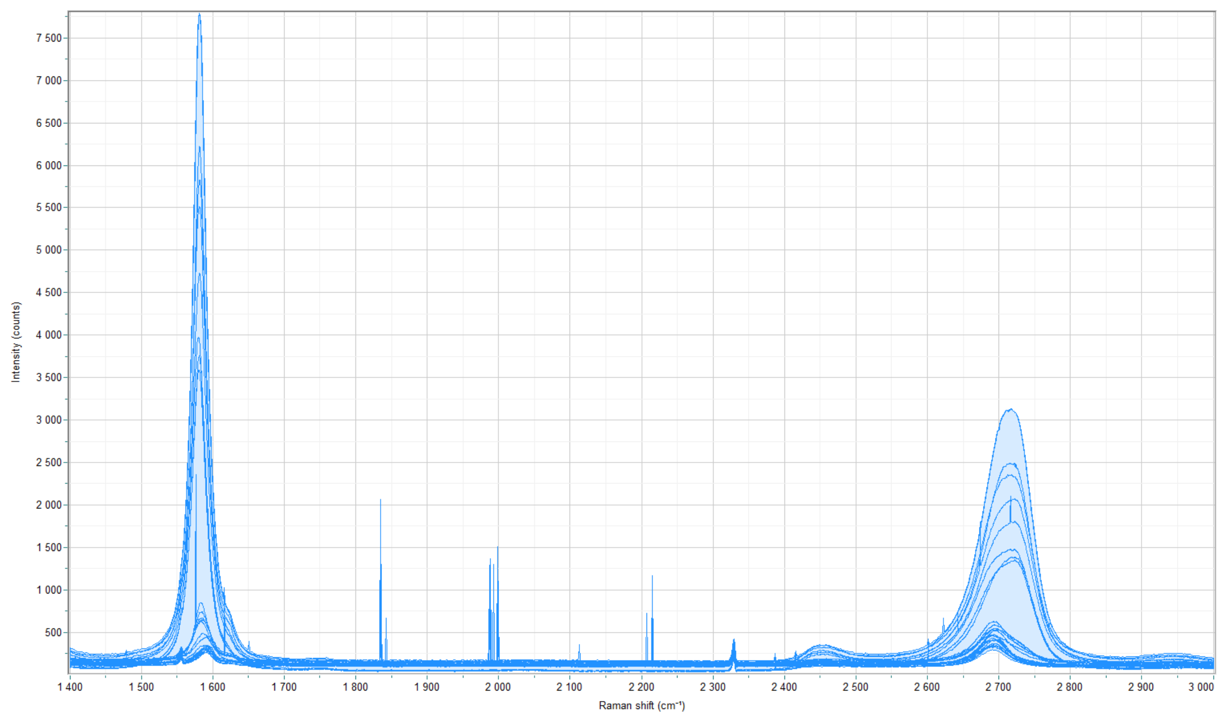

Figure B.2: The total Raman spectra of the top of structure C.5, resulting from the probing of 15 locations.

Appendix C

Table with experimental details

Table C.1: 8 micron device heated for 2 minutes.

Device	Voltage [V]	Current [I]	Cooling time [s]	Temperature [°C]	Top coverage	Sidewall coverage
A.5	0.44	3.37	0.5	1093	Mono: 15/15	Mono: 12/15 Bi: 1/15 Few: 1/15
C.4	0.45	3.39	0.5	1080	Few: 15/15	Mono: 8/15 Bi: 1/15 Few: 4/15
BNG.2	0.44	3.54	0.5	1049	Mono: 11/15 Bi: 1/15	Mono: 10/15 Bi: 1/15 Few: 2/15
BNG.6	0.43	3.81	0.5	1072	Mono: 12/15 Bi: 1/15 Few: 2/15	Mono: 8/15 Bi: 2/15 Few: 5/15
A3.8	0.44	3.27	0.5	996	Mono: 3/15 Bi:1/15 Few: 2/15	Mono: 9/15 Few: 4/15
B2.1	0.39	3.42	5	1084	Few: 6/15	Mono: 3/15 Bi: 2/15 Few: 4/15
B2.4	0.46	3.28	2	1086	Mono:2/15 Few: 3/15	Mono: 6/15 Bi: 4/15 Few: 3/15
B2.7	0.46	3.32	10	1084	Few: 6/15	Mono: 6/15 Bi: 2/15 Few: 3/15
C2.2	0.45	3.19	0.5	1036	Few: 6/15	Mono: 2/15 Bi: 1/15 Few: 3/15
C3.5	0.44	3.69	0.5	1022	-	Few: 2/15
B4.1	0.43	3.50	3	1110	Few: 3/15	Few: 6/15
B4.3	0.43	3.65	5.3	1052	Few: 3/15	Bi: 2/15 Few: 2/15
B4.5	0.44	3.85	0.5	1042	Mono: 1/15 Few: 4/15	Mono: 1/15 Few: 4/15

Table C.2: 8 micron device heated for 1 minute.

Device	Voltage [V]	Current [I]	Cooling time [s]	Temperature [°C]	Top coverage	Sidewall coverage
A2.6	0.44	3.44	0.5	1011	-	-
A3.2	0.43	3.60	0	1046	-	Mono: 8/15 Bi: 1/15 Few: 2/15
BNG.10	0.44	3.63	0.5	1047	Mono: 15/15	Mono: 13/15 Bi: 1/15

Table C.3: 6 micron device heated for 2 minutes.

Device	Voltage [V]	Current [I]	Cooling time [s]	Temperature [°C]	Top coverage	Sidewall coverage
A.6	0.49	3.53	0.5	1204	Mono: 11/18 Few: 7/18	Mono: 13/15 Bi: 1/15 Few: 1/15
C.5	0.46	3.17	0.5	1082	Mono: 5/15 Bi: 2/15 Few: 8/15	Mono: 10/15 Few: 5/15
BNG.4	0.40	3.26	0.5	995	Mono: 13/15 Few: 2/15	Mono: 14/15 Bi: 1/15
BNG.8	0.45	3.50	0.5	1072	Mono: 11/15 Bi: 1/15 Few: 2/15	Mono: 12/15 Bi: 1/15 Few: 2/15
A2.8	0.47	3.32	0.5	1143	Mono: 1/15 Few: 8/15	Few: 10/20
A3.6	0.47	3.58	0.5	1083	-	Mono: 10/15 Few: 3/15
B2.2	0.45	3.09	4	1024	Few: 5/15	Mono: 9/15 Bi: 2/15 Few: 2/15
B2.5	0.44	3.02	1.5	1030	Few: 2/15	Mono: 11/15 Bi: 1/15 Few: 2/15
B2.8	0.45	3.09	11	1040	Few: 6/15	Mono: 7/15 Few: 6/15
C2.1	0.44	3.08	1	998	Few: 6/15	Few: 4/15
C2.3	0.45	2.93	0.5	1026	Few: 6/15	Mono: 1/15 Few: 3/15
C3.3	0.41	3.09	0.5	924	Mono: 3/15	-
C3.4	0.41	3.30	0.5	950	-	Few: 2/15
B4.2	0.42	3.22	6	982	Few: 2/15	Few: 6/15
B4.4	0.44	3.35	4	1024	Bi: 3/15 Few: 1/15	Bi:1/15 Few: 4/15

Table C.4: 6 micron device heated for 1 minute.

Device	Voltage [V]	Current [I]	Cooling time [s]	Temperature [°C]	Top coverage	Sidewall coverage
A3.4	0.46	3.45	0	1072	Few: 3/15	Mono: 9/15 Few: 4/15
BNG.12	0.41	3.38	0.5	1006	Mono: 5/15 Bi: 3/15 Few: 4/15	Mono: 8/15 Bi: 3/15 Few: 3/15

Table C.5: Alternating current experiments with 6 and 8 µmdevices heated for 2 minutes at high temperature.

Device	Size [µm]	Voltage [V]	Current [I]	Frequency alternating current [Hz]	Cooling time [s]	Temperature [°C]	Top coverage	Sidewall coverage
A4.1	8	0.44	3.33	0.03	10	1025	Few: 5/15	Mono: 3/15 Few: 6/15
A4.2	8	0.43	3.40	1	10	1001	Few: 3/15	Bi: 2/15 Few: 7/15
A4.3	6	0.44	3.13	1	8	1001	Mono: 1/15 Few: 5/15	Mono: 1/15 Few: 7/15
A4.4	6	0.43	3.06	0.03	8	1028	Mono: 1/15 Few: 5/15	Bi: 2/15 Few: 6/15

Table C.6: Post annealing experiments with 6 and 8 µmdevices heated for 1 minute in argon at high temperature.

Device	Size [µm]	Voltage [V]	Current [I]	Cooling time [s]	Temperature [°C]	Top coverage	Sidewall coverage
BNG.2	8	0.45	3.43	0.5	1049	-	-
BNG.4	6	0.43	3.00	0.5	995	Few: 5/15	Mono: 1/15 Bi: 1/15 Few: 5/15
BNG.6	8	0.43	3.80	0.5	1072	-	-
BNG.8	6	0.46	3.46	0.5	1072	-	Few: 3/15
BNG.10	8	0.45	3.60	0.5	1047	-	Few: 1/15
BNG.12	6	0.42	3.31	0.5	1006	Bi: 1/15	Few: 2/15

Appendix D

Setup details

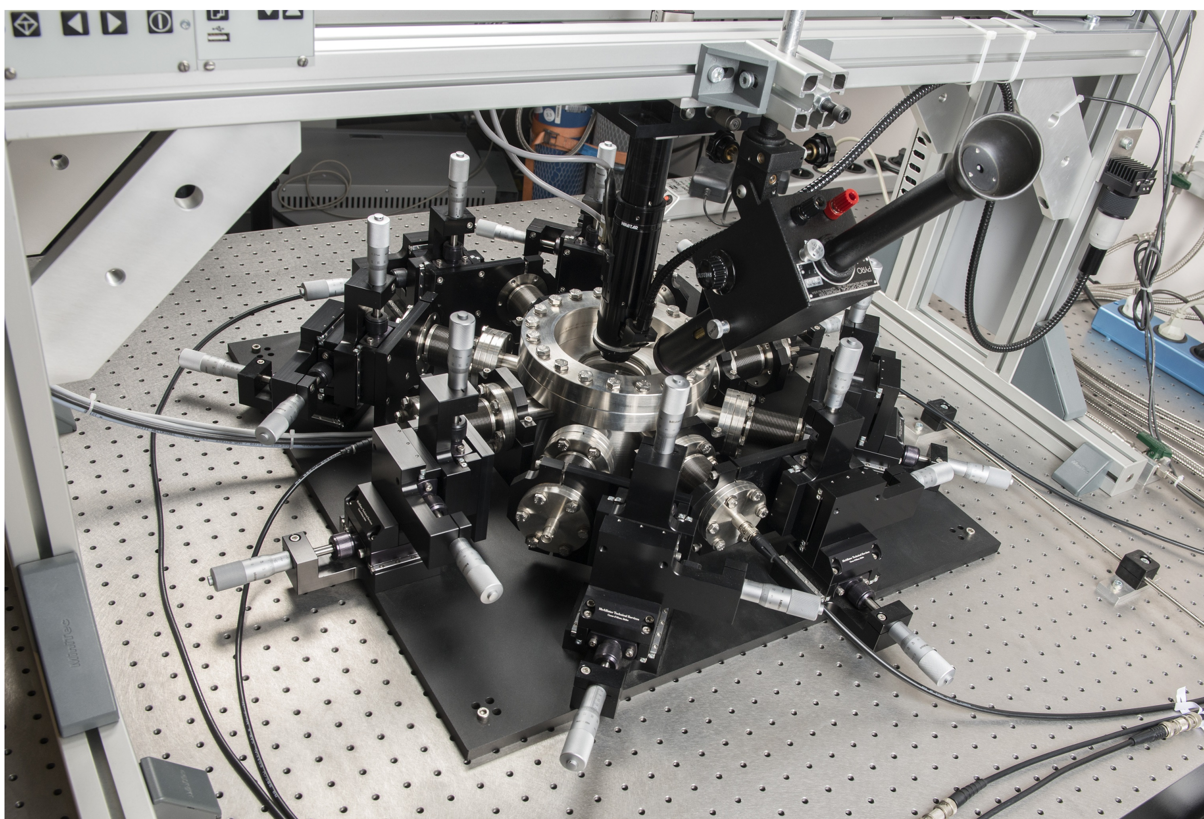

Figure D.1: The probe station

Figure D.2: Detailed picture of the probe station with a chip inside

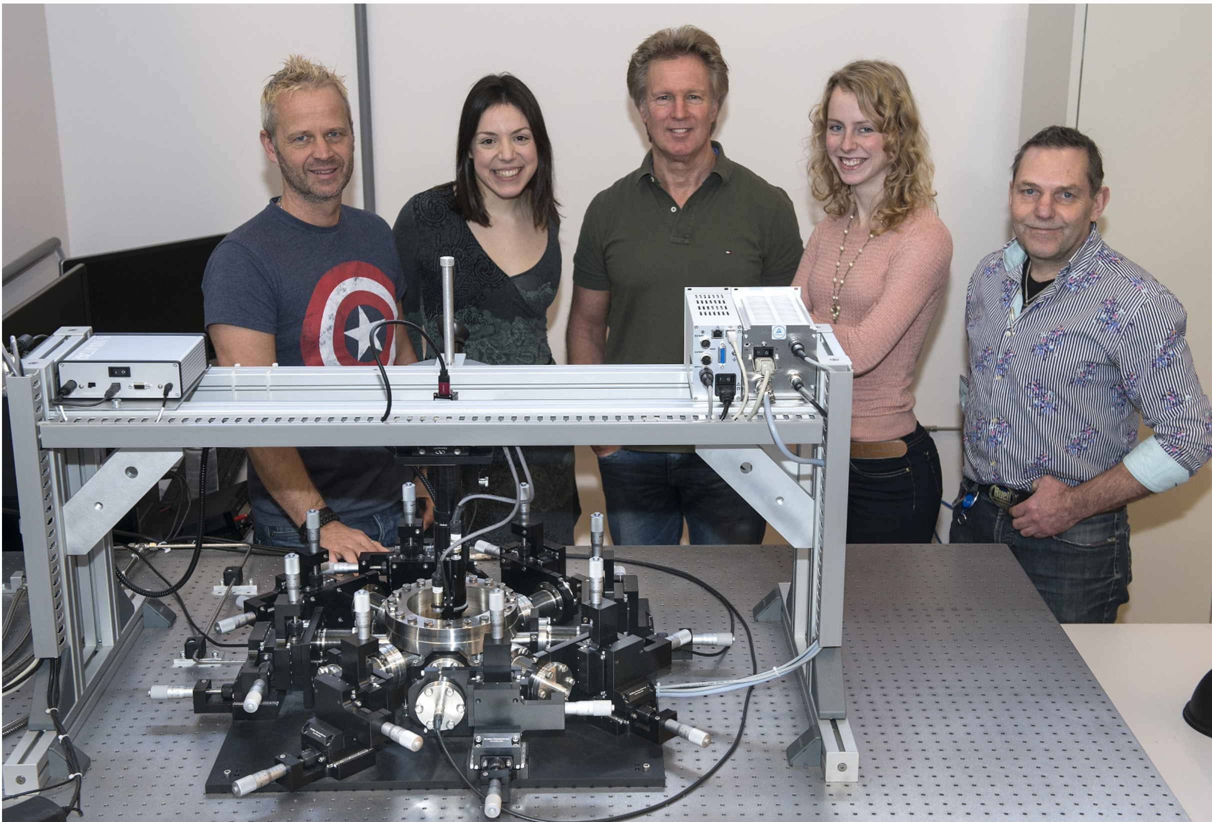

Figure D.3: The probe station with the technicians who made it to work

Bibliography

[1] HG Phakatkar and RR Ghorpade. *Tribology.* Nirali Prakashan, Pune, 2nd edition, 2009.

[2] Danelle M Tanner, Norman F Smith, Lloyd W irwin, William P Eaton, Karen Sue Helgesen, J Joseph Clement, William M Miller, Samuel L Miller, Michael T Dugger, Jeremy A Walraven, et al. Mems reliability: infrastructure, test structures, experiments, and failure modes. Technical report, Sandia National Labs., Albuquerque, NM (US); Sandia National Labs., Livermore, CA (US), 2000.

[3] Seong H Kim, David B Asay, and Michael T Dugger. Nanotribology and mems. *Nano today*, 2(5):22–29, 2007.

[4] Nicolas Argibay, James H Keith, Brandon A Krick, DW Hahn, Gerald R Bourne, and W Gregory Sawyer. High-temperature vapor phase lubrication using carbonaceous gases. *Tribology letters*, 40(1):3–9, 2010.

[5] David B Asay, Michael T Dugger, and Seong H Kim. In-situ vapor-phase lubrication of mems. *Tribology Letters*, 29(11):67–7, 2008.

[6] Seong H Kim. Vapor phase lubrication for micro-machines. In *Encyclopedia of Tribology*, pages 3960–3966. Springer, 2013.

[7] JA Williams and HR Le. Tribology and mems. *Journal of Physics D: Applied Physics*, 39(12):R201, 2006.

[8] Bharat Bhushan. Nanotribology and nanomechanics. *Wear*, 259(7):1507–1531, 2005.

[9] Roya Maboudian, W Robert Ashurst, and Carlo Carraro. Self-assembled monolayers as anti-stiction coatings for mems: characteristics and recent developments. *Sensors and Actuators A: Physical*, 82(1):219–223, 2000.

[10] Bharat Bhushan and Huiwen Liu. Nanotribological properties and mechanisms of alkylthiol and biphenyl thiol self-assembled monolayers studied by afm. *Physical Review B*, 63(24):245412, 2001.

[11] Said Jahanmir, Y Ozmen, and LK Ives. Water lubrication of silicon nitride in sliding. *Tribology Letters*, 17(3):409–417, 2004.

[12] Min Dai, Yu Wang, Jinhee Kwon, Mathew D Halls, and Yves J Chabal. Nitrogen interaction with hydrogen-terminated silicon surfaces at the atomic scale. *Nature materials*, 8(10):825–830, 2009.

[13] Roya Maboudian, W Robert Ashurst, and Carlo Carraro. Tribological challenges in micromechanical systems. *Tribology letters*, 12(2):95–100, 2002.

[14] Michael R Houston, Roger T Howe, and Roya Maboudian. Effect of hydrogen termination on the work of adhesion between rough polycrystalline silicon surfaces. *Journal of applied physics*, 81(8):3474–3483, 1997.

[15] IA Dogel, SA Dogel, JL Pitters, GA DiLabio, and RA Wolkow. Chemical methods for the hydrogen termination of silicon dangling bonds. *Chemical Physics Letters*, 448(4):237–242, 2007.

[16] John J Boland. Scanning tunnelling microscopy of the interaction of hydrogen with silicon surfaces. *Advances in physics*, 42(2):129–171, 1993.

[17] Baiming Chen, Qinling Bi, Jun Yang, Yanqiu Xia, and Jingcheng Hao. Tribological properties of solid lubricants (graphite, h-bn) for cu-based p/m friction composites. *Tribology international*, 41(12):1145–1152, 2008.

[18] Li Song, Lijie Ci, Hao Lu, Pavel B Sorokin, Chuanhong Jin, Jie Ni, Alexander G Kvashnin, Dmitry G Kvashnin, Jun Lou, Boris I Yakobson, et al. Large scale growth and characterization of atomic hexagonal boron nitride layers. *Nano letters*, 10(8):3209–3215, 2010.

[19] Kang Hyuck Lee, Hyeon-Jin Shin, Jinyeong Lee, In-yeal Lee, Gil-Ho Kim, Jae-Young Choi, and Sang-Woo Kim. Large-scale synthesis of high-quality hexagonal boron nitride nanosheets for large-area graphene electronics. *Nano letters*, 12(2):714–718, 2012.

[20] Shuichi Watanabe, Shojiro Miyake, and Masao Murakawa. Tribological properties of cubic, amorphous and hexagonal boron nitride films. *Surface and Coatings Technology*, 49(1-3):406–410, 1991.

[21] Changhong Cao, Yu Sun, and Tobin Filleter. Characterizing mechanical behavior of atomically thin films: A review. *Journal of Materials Research*, 29(03):338–347, 2014.

[22] Yang Gao, Wencai Ren, Teng Ma, Zhibo Liu, Yu Zhang, Wen-Bin Liu, Lai-Peng Ma, Xiuliang Ma, and Hui-Ming Cheng. Repeated and controlled growth of monolayer, bilayer and few-layer hexagonal boron nitride on pt foils. *ACS nano*, 7(6):5199–5206, 2013.

[23] Robert L Fusaro. Lubrication and failure mechanisms of molybdenum disulfide films. 1: Effect of atmosphere. 1978.

[24] R Holinski and J Gänsheimer. A study of the lubricating mechanism of molybdenum disulfide. *Wear*, 19(3):329–342, 1972.

[25] WO Winer. Molybdenum disulfide as a lubricant: a review of the fundamental knowledge. *Wear*, 10(6):422–452, 1967.

[26] WJ Schutte, JL De Boer, and F Jellinek. Crystal structures of tungsten disulfide and diselenide. *Journal of Solid State Chemistry*, 70(2):207–209, 1987.

[27] Chuanqi Feng, Lunfeng Huang, Zaiping Guo, and Huakun Liu. Synthesis of tungsten disulfide (ws 2) nanoflakes for lithium ion battery application. *Electrochemistry communications*, 9(1):119–122, 2007.

[28] SV Prasad, NT McDevitt, and JS Zabinski. Tribology of tungsten disulfide–nanocrystalline zinc oxide adaptive lubricant films from ambient to 500 c. *Wear*, 237(2):186–196, 2000.

[29] SV Prasad, NT McDevitt, and JS Zabinski. Tribology of tungsten disulfide films in humid environments:: The role of a tailored metal-matrix composite substrate. *Wear*, 230(1):24–34, 1999.

[30] TW Scharf, SV Prasad, MT Dugger, PG Kotula, RS Goeke, and RK Grubbs. Growth, structure, and tribological behavior of atomic layer-deposited tungsten disulphide solid lubricant coatings with applications to mems. *Acta materialia*, 54(18):4731–4743, 2006.

[31] Bharat Bhushan. Nanotribology and nanomechanics of mems/nems and biomems/bionems materials and devices. *Microelectronic Engineering*, 84(3):387–412, 2007.

[32] JK Luo, YQ Fu, HR Le, JA Williams, SM Spearing, and WI Milne. Diamond and diamond-like carbon mems. *Journal of Micromechanics and Microengineering*, 17(7):S147, 2007.

[33] Hongjun Zeng, Andrew R Konicek, Nicolaie Moldovan, Filippo Mangolini, Tevis Jacobs, Ian Wylie, Prabhu U Arumugam, Shabnam Siddiqui, Robert W Carpick, and John A Carlisle. Boron-doped ultrananocrystalline diamond synthesized with an h-rich/ar-lean gas system. *Carbon*, 84:103–117, 2015.

[34] Qi Liang, Andrei Stanishevsky, and Yogesh K Vohra. Tribological properties of undoped and boron-doped nanocrystalline diamond films. *Thin Solid Films*, 517(2):800–804, 2008.

[35] Federico Buja, Jaap Kokorian, Anirudha V Sumant, and W Merlijn van Spengen. Studies on measuring surface adhesion between sidewalls in boron doped ultrananocrystalline diamond based microelectromechanical devices. *Diamond and Related Materials*, 55:22–31, 2015.

[36] PJ Bryant, PL Gutshall, and LH Taylor. A study of mechanisms of graphite friction and wear. *Wear*, 7(1):118–126, 1964.

[37] Quanshun Luo. Tribofilms in solid lubricants. *Encyclopedia of Tribology*, pages 3760–3767, 2013.

[38] John Spreadborough. The frictional behaviour of graphite. *Wear*, 5(1):18–30, 1962.

[39] Martin Dienwiebel, Namboodiri Pradeep, Gertjan S Verhoeven, Henny W Zandbergen, and Joost WM Frenken. Model experiments of superlubricity of graphite. *Surface Science*, 576(1):197–211, 2005.

[40] Diana Berman, Ali Erdemir, and Anirudha V Sumant. Graphene: a new emerging lubricant. *Materials Today*, 17(1):31–42, 2014.

[41] Oleksiy Penkov, Hae-Jin Kim, Hyun-Joon Kim, and Dae-Eun Kim. Tribology of graphene: a review. *International journal of precision engineering and manufacturing*, 15(3):577–585, 2014.

[42] Changgu Lee, Xiaoding Wei, Jeffrey W Kysar, and James Hone. Measurement of the elastic properties and intrinsic strength of monolayer graphene. *science*, 321(5887):385–38, 2008.

[43] Kazumasa Shinjo and Motohisa Hirano. Dynamics of friction: superlubric state. *Surface Science*, 283(1-3):473–478, 1993.

[44] Diana Berman, Sanket A Deshmukh, Subramanian KRS Sankaranarayanan, Ali Erdemir, and Anirudha V Sumant. Macroscale superlubricity enabled by graphene nanoscroll formation. *Science*, 348(6239):1118–1122, 2015.

[45] Kostya S Novoselov, Andre K Geim, Sergei V Morozov, D Jiang, Y_ Zhang, Sergey V Dubonos, Irina V Grigorieva, and Alexandr A Firsov. Electric field effect in atomically thin carbon films. *science*, 306(5696):666–669, 2004.

[46] Urmimala Maitra, HSS Matte, Prashant Kumar, and CNR Rao. Strategies for the synthesis of graphene, graphene nanoribbons, nanoscrolls and related materials. *CHIMIA International Journal for Chemistry*, 66(12):941–948, 2012.

[47] Dmitry V Kosynkin, Amanda L Higginbotham, Alexander Sinitskii, Jay R Lomeda, Ayrat Dimiev, B Katherine Price, and James M Tour. Longitudinal unzipping of carbon nanotubes to form graphene nanoribbons. *Nature*, 458(7240):872–876, 2009.

[48] Liying Jiao, Li Zhang, Xinran Wang, Georgi Diankov, and Hongjie Dai. Narrow graphene nanoribbons from carbon nanotubes. *Nature*, 458(7420):877–880, 2009.

[49] S Mohammadi, Z Kolahdouz, S Darbari, S Mohajerzadeh, and N Masoumi. Graphene formation by unzipping carbon nanotubes using a sequential plasma assisted processing. *Carbon*, 52:451–463, 2013.

[50] Sehmus Ozden, Pedro AS Autreto, Chandra Sekhar Tiwary, Suman Khatiwada, Leonardo Machado, Douglas S Galvao, Robert Vajtai, Enrique V Barrera, and Pulickel M. Ajayan. Uzipping carbon nanotubes at high impact. *Nano Letters*, 14(7):4131–4137, 2014.

[51] Liang Ma, Jinlan Wang, and Feng Ding. Recent progress and challenges in graphene nanoribbon synthesis. *ChemPhysChem*, 14(1):47–54, 2013.

[52] SR Dhakate, N Chauhan, S Sharma, and RB Mathur. The production of multi-layer graphene nanoribbons from thermally reduced unzipped multi-walled carbon nanotubes. *Carbon*, 49(13):4170–4178, June 2011.

[53] KS Subrahmanyam, LS Panchakarla, A Govindaraj, and CNR Rao. Simple method of preparing graphene flakes by an arc-discharge method. *The Journal of Physical Chemistry C*, 113(11):4257–4259, 2009.

[54] Chuxin Wu, Guofa Dong, and Lunhui Guan. Production of graphene sheets by a simple helium arc-discharge. *Physica E: Low-dimensional Systems and Nanostructures*, 42(5):1267–1271, 2010.

[55] Yingpeng Wu, Tengfei Zhang, Fan Zhang, Yan Wang, Yanfeng Ma, Yi Huang, Yiyang Liu, and Yongsheng Chen. In situ synthesis of graphene/single-walled carbon nanotube hybrid material by arc-discharge and its application in supercapacitors. *Nano Energy*, 1(6):820–827, 2012.

[56] Yingpeng Wu, Bin Wang, Yanfeng Ma, Yi Huang, Na Li, Fan Zhang, and Yongsheng Chen. Efficient and large-scale synthesis of few-layered graphene using an arc-discharge method and conductivity studies of the resulting films. *Nano Research*, 3(9):661–669, 2010.

[57] Veena Choudhary, BP Singh, and RB Mathur. Carbon nanotubes and their composites. *Syntheses and applications of carbon nanotubes and their composites. InTech, Rijeka ISBN*, pages 978–953, 2013.

[58] Konstantin V Emtsev, Aaron Bostwick, Karsten Horn, Johannes Jobst, Gary L Kellogg, Lothar Ley, Jessica L McChesney, Taisuke Ohta, Sergey A Reshanov, Jonas Röhrl, et al. Towards wafer-size graphene layers by atmospheric pressure graphitization of silicon carbide. *Nature materials*, 8(3):203–207, 2009.

[59] Claire Berger, Zhimin Song, Xuebin Li, Xiaosong Wu, Nate Brown, Cécile Naud, Didier Mayou, Tianbo Li, Joanna Hass, Alexei N Marchenkov, et al. Electronic confinement and coherence in patterned epitaxial graphene. *Science*, 312(5777):1191–1196, 2006.

[60] I Forbeaux, J-M Themlin, A Charrier, F Thibaudau, and J-M Debever. Solid-state graphitization mechanisms of silicon carbide 6h–sic polar faces. *Applied surface science*, 162:406–412, 2000.

[61] C Riedl, C Coletti, and U Starke. Structural and electronic properties of epitaxial graphene on sic (0 0 0 1): a review of growth, characterization, transfer doping and hydrogen intercalation. *Journal of Physics D: Applied Physics*, 43(37):374009, 2010.

[62] Nishtha Srivastava, Guowei He, Patrick C Mende, Randall M Feenstra, Yugang Sun, et al. Graphene formed on sic under various environments: comparison of si-face and c-face. *Journal of Physics D: Applied Physics*, 45(15):154001, 2012.

[63] Wei-Wen Liu, Siang-Piao Chai, Abdul Rahman Mohamed, and U Hashim. Synthesis and characterization of graphene and carbon nanotubes: A review on the past and recent developments. *Journal of Industrial and Engineering Chemistry*, 20(4):1171–118, 2014.

[64] Wataru Norimatsu and Michiko Kusunoki. Epitaxial graphene on sic {0001}: advances and perspectives. *Physical Chemistry Chemical Physics*, 16(8):3501–3511, 2014.

[65] JB Hannon and RM Tromp. Pit formation during graphene synthesis on sic (0001): In situ electron microscopy. *Physical review B*, 77(24):241404, 2008.

[66] William S Hummers Jr and Richard E Offeman. Preparation of graphitic oxide. *Journal of the American Chemical Society*, 80(6):1339–1339, 1958.

[67] Shaw Yong Toh, Kee Shyuan Loh, Siti Kartom Kamarudin, and Wan Ramli Wan Daud. Graphene production via electrochemical reduction of graphene oxide: synthesis and characterisation. *Chemical Engineering Journal*, 251:422–434, 2014.

[68] Hannes C Schniepp, Je-Luen Li, Michael J McAllister, Hiroaki Sai, Margarita Herrera-Alonso, Douglas H Adamson, Robert K Prud'homme, Roberto Car, Dudley A Saville, and Ilhan A Aksay. Functionalized single graphene sheets derived from splitting graphite oxide. *The Journal of Physical Chemistry B*, 110(17):8535–8539, 2006.

[69] Jeremy T Robinson, Maxim Zalalutdinov, Jeffrey W Baldwin, Eric S Snow, Zhongqing Wei, Paul Sheehan, and Brian H Houston. Wafer-scale reduced graphene oxide films for nanomechanical devices. *Nano letters*, 8(10):3441–3445, 2008.

[70] Sasha Stankovich, Dmitriy A Dikin, Richard D Piner, Kevin A Kohlhaas, Alfred Kleinhammes, Yuanyuan Jia, Yue Wu, SonBinh T Nguyen, and Rodney S Ruoff. Synthesis of graphene-based nanosheets via chemical reduction of exfoliated graphite oxide. *Carbon*, 45(7):1558–1565, 2007.

[71] Rajni Garg, Naba K Dutta, and Namita Roy Choudhury. Work function engineering of graphene. *Nanomaterials*, 4(2):267–300, 2014.

[72] Jussi Kauppila, Peter Kunnas, Pia Damlin, Antti Viinikanoja, and Carita Kvarnström. Electrochemical reduction of graphene oxide films in aqueous and organic solutions. *Electrochimica Acta*, 89:84–89, 2013.

[73] Ming Zhang, Bin Gao, Diana C Vanegas, Eric S McLamore, June Fang, Lin Liu, Lei Wu, and Hao Chen. Simple approach for large-scale production of reduced graphene oxide films. *Chemical engineering journal*, 243:340–346, 2014.

[74] Yupeng Zhang, Delong Li, Xiaojian Tan, Bin Zhang, Xuefeng Ruan, Huijun Liu, Chunxu Pan, Lei Liao, Tianyou Zhai, Yoshio Bando, et al. High quality graphene sheets from graphene oxide by hot-pressing. *Carbon*, 54:143–148, 2013.

[75] O Akhavan and E Ghaderi. Photocatalytic reduction of graphene oxide nanosheets on tio2 thin film for photoinactivation of bacteria in solar light irradiation. *The Journal of Physical Chemistry C*, 113(47):20214–20220, 2009.

[76] Mahesh Agharkar, Sachin Kochrekar, Slah Hidouri, and Musibau A Azeez. Trends in green reduction of graphene oxides, issues and challenges: a review. *Materials Research Bulletin*, 59:323–328, 2014.

[77] Jian Gao, Fang Liu, Yiliu Liu, Ning Ma, Zhiqiang Wang, and Xi Zhang. Environment-friendly method to produce graphene that employs vitamin c and amino acid. *Chemistry of Materials*, 22(7):2213–2218, 2010.

[78] Zhuangjun Fan, Kai Wang, Tong Wei, Jun Yan, Liping Song, and Bo Shao. An environmentally friendly and efficient route for the reduction of graphene oxide by aluminum powder. *Carbon*, 48(5):1686 – 1689, 2010.

[79] F Ostovari, Y Abdi, S Darbari, and F Ghasemi. Effects of electrochemical resonance on photocatalytic reduction of the free-hanging graphene oxide sheets. *Journal of nanoparticle research*, 15(4):1–9, 2013.

[80] Priyank V Kumar, Neelkanth M Bardhan, Guan-Yu Chen, Zeyang Li, Angela M Belcher, and Jeffrey C Grossman. New insights into the thermal reduction of graphene oxide: Impact of oxygen clustering. *Carbon*, 100:90–98, 2016.

[81] JC Shelton, HR Patil, and JM Blakely. Equilibrium segregation of carbon to a nickel (111) surface: A surface phase transition. *Surface Science*, 43(2):493–520, 1974.

[82] Qin Zhou and Liwei Lin. Synthesis of graphene using micro chemical vapor deposition. In *IEEE 23rd International Conference on Micro Electro Mechanical Systems*, pages 43–46, 2010.

[83] Gang Wang, Miao Zhang, Yun Zhu, Guqiao Ding, Da Jiang, Qinglei Guo, Su Liu, Xiaoming Xie, Paul K Chu, Zengfeng Di, et al. Direct growth of graphene film on germanium substrate. *Scientific reports*, 3, 2013.

[84] TA Land, Th Michely, RJ Behm, JC Hemminger, and G Comsa. Stm investigation of single layer graphite structures produced on pt (111) by hydrocarbon decomposition. *Surface Science*, 264(3):261–270, 1992.

[85] Yi Zhang, Lewis Gomez, Fumiaki N Ishikawa, Anuj Madaria, Koungmin Ryu, Chuan Wang, Alexander Badmaev, and Chongwu Zhou. Comparison of graphene growth on single-crystalline and polycrystalline ni by chemical vapor deposition. *The Journal of Physical Chemistry Letters*, 1(20):3101–3107, 2010.

[86] Igor Levchenko, Kostya Ken Ostrikov, Jie Zheng, Xingguo Li, Michael Keidar, and Kenneth BK Teo. Scalable graphene production: perspectives and challenges of plasma applications. *Nanoscale*, 8(20):10511–10527, 2016.

[87] Roumen Vitchev, Alexander Malesevic, Roumen H Petrov, Raymond Kemps, Myrjam Mertens, Annick Vanhulsel, and Chris Van Haesendonck. Initial stages of few-layer graphene growth by microwave plasma-enhanced chemical vapour deposition. *Nanotechnology*, 21(9):095602, 2010.

[88] KM Al-Shurman and Hameed Naseem. Cvd graphene growth mechanism on nickel thin films. In *Proceedings of the 2014 COMSOL Conference in Boston*, 2014.

[89] Wei Wu, Qingkai Yu, Peng Peng, Zhihong Liu, Jiming Bao, and Shin-Shem Pei. Control of thickness uniformity and grain size in graphene films for transparent conductive electrodes. *Nanotechnology*, 23(3):035603, 2011.

[90] Vaidotas Miseikis, Domenica Convertino, Neeraj Mishra, Mauro Gemmi, Torge Mashoff, Stefan Heun, Niloofar Haghighian, Francesco Bisio, Maurizio Canepa, Vincenzo Piazza, et al. Rapid cvd growth of millimetre-sized single crystal graphene using a cold-wall reactor. *2D Materials*, 2(1):014006, 2015.

[91] Keun Soo Kim, Yue Zhao, Houk Jang, Sang Yoon Lee, Jong Min Kim, Kwang S Kim, Jong-Hyun Ahn, Philip Kim, Jae-Young Choi, and Byung Hee Hong. Large-scale pattern growth of graphene films for stretchable transparent electrodes. *Nature*, 457(7230):706–710, 2009.

[92] L Baraton, ZB He, CS Lee, CS Cojocaru, M Châtelet, J-L Maurice, YH Lee, and D Pribat. On the mechanisms of precipitation of graphene on nickel thin films. *EPL (Europhysics Letters)*, 96(4):46003, 2011.

[93] MEMSCAP. Mumps. `http://www.memscap.com/products/mumps`; Accessed at 16 February 2017.

[94] Vitaliy Babenko, Adrian T Murdock, Antal A Koós, Jude Britton, Alison Crossley, Philip Holdway, Jonathan Moffat, Jian Huang, Jack A Alexander-Webber, Robin J Nicholas, et al. Rapid epitaxy-free graphene synthesis on silicidated polycrystalline platinum. *Nature communications*, 6, 2015.

[95] Engineering Toolbox. Metals - melting temperatures. `http://www.engineeringtoolbox.com/melting-temperature-metals-d_860.html`; Accessed at 20 February 2017.

[96] Iwona Pasternak, Marek Wesolowski, Iwona Jozwik, Mindaugas Lukosius, Grzegorz Lupina, Pawel Dabrowski, Jacek M Baranowski, and Wlodek Strupinski. Graphene growth on ge (100)/si (100) substrates by cvd method. *Scientific reports*, 6, 2016.

[97] Menglin Li, Donghua Liu, Dacheng Wei, Xuefen Song, Dapeng Wei, and Andrew Thye Shen Wee. Controllable synthesis of graphene by plasma-enhanced chemical vapor deposition and its related applications. *Advanced Science*, 2016.

[98] JJ Wang, MY Zhu, RA Outlaw, X Zhao, DM Manos, BC Holloway, and VP Mammana. Free-standing subnanometer graphite sheets. *Applied Physics Letters*, 85(7):1265–1267, 2004.

[99] Mingyao Zhu, Jianjun Wang, Brian C Holloway, RA Outlaw, Xin Zhao, Kun Hou, V Shutthanandan, and Dennis M Manos. A mechanism for carbon nanosheet formation. *Carbon*, 45(11):2229–2234, 2007.

[100] Ivan Vlassiouk, Murari Regmi, Pasquale Fulvio, Sheng Dai, Panos Datskos, Gyula Eres, and Sergei Smirnov. Role of hydrogen in chemical vapor deposition growth of large single-crystal graphene. *ACS nano*, 5(7):6069–6076, 2011.

[101] Ivan Vlassiouk, Pasquale Fulvio, Harry Meyer, Nick Lavrik, Sheng Dai, Panos Datskos, and Sergei Smirnov. Large scale atmospheric pressure chemical vapor deposition of graphene. *Carbon*, 54:58–67, 2013.

[102] Jungtae Nam, Dong-Chul Kim, Hoyeol Yun, Dong Hoon Shin, Seungjin Nam, Won Ki Lee, Jun Yeon Hwang, Sang Wook Lee, Helge Weman, and Keun Soo Kim. Chemical vapor deposition of graphene on platinum: Growth and substrate interaction. *Carbon*, 111:733–740, 2017.

[103] Miriam Marchena, Davide Janner, Tong Lai Chen, Vittoria Finazzi, and Valerio Pruneri. Low temperature direct growth of graphene patterns on flexible glass substrates catalysed by a sacrificial ultrathin ni film. *Optical Materials Express*, 6(8):2487–2507, 2016.

[104] Yagang Yao and Ching-ping Wong. Monolayer graphene growth using additional etching process in atmospheric pressure chemical vapor deposition. *Carbon*, 50(14):5203–5209, 2012.

[105] Alfonso Reina, Stefan Thiele, Xiaoting Jia, Sreekar Bhaviripudi, Mildred S Dresselhaus, Juergen A Schaefer, and Jing Kong. Growth of large-area single-and bi-layer graphene by controlled carbon precipitation on polycrystalline ni surfaces. *Nano Research*, 2(6):509–516, 2009.

[106] Phaedon Avouris and Christos Dimitrakopoulos. Graphene: synthesis and applications. *Materials today*, 15(3):86–97, 2012.

[107] Seung Jin Chae, Fethullah Güneş, Ki Kang Kim, Eun Sung Kim, Gang Hee Han, Soo Min Kim, Hyeon-Jin Shin, Seon-Mi Yoon, Jae-Young Choi, Min Ho Park, et al. Synthesis of large-area graphene layers on poly-nickel substrate by chemical vapor deposition: wrinkle formation. *Advanced Materials*, 21(22):2328–2333, 2009.

[108] Matthias Batzill. The surface science of graphene: Metal interfaces, cvd synthesis, nanoribbons, chemical modifications, and defects. *Surface Science Reports*, 67(3):83–115, 2012.

[109] Hye Jin Park, Jannik Meyer, Siegmar Roth, and Viera Skákalová. Growth and properties of few-layer graphene prepared by chemical vapor deposition. *Carbon*, 48(4):1088–1094, 2010.

[110] J Marquez Velasco, SA Giamini, N Kelaidis, P Tsipas, D Tsoutsou, G Kordas, YS Raptis, N Boukos, and A Dimoulas. Reducing the layer number of ab stacked multilayer graphene grown on nickel by annealing at low temperature. *Nanotechnology*, 26(40):405603, 2015.

[111] Roberto Muñoz and Cristina Gómez-Aleixandre. Review of cvd synthesis of graphene. *Chemical Vapor Deposition*, 19(10-11-12):297–322, 2013.

[112] Maria Losurdo, Maria Michela Giangregorio, Pio Capezzuto, and Giovanni Bruno. Graphene cvd growth on copper and nickel: role of hydrogen in kinetics and structure. *Physical Chemistry Chemical Physics*, 13(46):20836–20843, 2011.

[113] QH Chang, GL Guo, T Wang, LC Ji, L Huang, B Ling, and HF Yang. Few-layer graphene direct deposition on ni andcu foil by cold-wall chemical vapor deposition. *Journal of nanoscience and nanotechnology*, 12(8):6516–6520, 2012.

[114] Amanda Lewis. Fundamental studies of the chemical vapour deposition of graphene on copper. 2014.

[115] Wei Liu, Choong-Heui Chung, Cong-Qin Miao, Yan-Jie Wang, Bi-Yun Li, Ling-Yan Ruan, Ketan Patel, Young-Ju Park, Jason Woo, and Ya-Hong Xie. Chemical vapor deposition of large area few layer graphene on si catalyzed with nickel films. *Thin Solid Films*, 518(6):S128–S132, 2010.

[116] Xianglian Song, Lixin Song, Xiaoying Chen, and Tao Zhang. The characterization of graphene prepared using a nickel film catalyst pre-deposited to fused silica. *RSC Adv.*, 6:22244–22249, 2016.

[117] Seon Joon Kim, Dae Woo Kim, and Hee-Tae Jung. Key growth parameters affecting the domain structure of chemical vapor deposition (cvd)-grown graphene on nickel. *Rsc Advances*, 3(45):22909–22913, 2013.

[118] L Huang, QH Chang, GL Guo, Y Liu, YQ Xie, T Wang, B Ling, and HF Yang. Synthesis of high-quality graphene films on nickel foils by rapid thermal chemical vapor deposition. *Carbon*, 50(2):551–556, 2012.

[119] Yi Zhang, Zhen Li, Pyojae Kim, Luyao Zhang, and Chongwu Zhou. Anisotropic hydrogen etching of chemical vapor deposited graphene. *ACS nano*, 6(1):126–132, 2011.

[120] Daniel Q McNerny, B Viswanath, Davor Copic, Fabrice R Laye, Christophor Prohoda, Anna C Brieland-Shoultz, Erik S Polsen, Nicholas T Dee, Vijayen S Veerasamy, and A John Hart. Direct fabrication of graphene on sio2 enabled by thin film stress engineering. *Scientific reports*, 4:5049, 2014.

[121] Pyro. *MicroTherm Datasheet*.

[122] Fran Cverna et al. *ASM ready reference: thermal properties of metals*. ASM International, 2002.

[123] Allen Cowen, Bruce Dudley, E Hill, M Walters, R Wood, S Johnson, H Wynands, and B Hardy. Metalmumps design handbook. *MEMSCAP revision*, 1, 2002.

[124] Congqin Miao, Churan Zheng, Owen Liang, and Ya-Hong Xie. Chemical vapor deposition of graphene. In *Physics and applications of graphene-experiments*. InTech, 2011.

[125] MA Pimenta, G Dresselhaus, Mildred S Dresselhaus, LG Cancado, Ado Jorio, and R Saito. Studying disorder in graphite-based systems by raman spectroscopy. *Physical chemistry chemical physics*, 9(11):1276–1290, 2007.

[126] Anindya Das, Biswanath Chakraborty, and AK Sood. Raman spectroscopy of graphene on different substrates and influence of defects. *Bulletin of Materials Science*, 31(3):579–584, 2008.

[127] Arjun Dahal and Matthias Batzill. Graphene–nickel interfaces: a review. *Nanoscale*, 6(5):2548–2562, 2014.

[128] Engineering Toolbox. Thermal conductivity of common materials and gases. `http://www.engineeringtoolbox.com/thermal-conductivity-d_429.html`; Accessed at 26 July 2017.

[129] Srikrishna C Bodepudi, Abhay P Singh, and Sandipan Pramanik. Current-perpendicular-to-plane magnetoresistance in chemical vapor deposition-grown multilayer graphene. *Electronics*, 2(3):315–331, 2013.

[130] Isaac Childres, Luis A Jauregui, Wonjun Park, Helin Cao, and Yong P Chen. Raman spectroscopy of graphene and related materials. *New developments in photon and materials research*, pages 1–20, 2013.

[131] Daniel R Lenski and Michael S Fuhrer. Raman and optical characterization of multilayer turbostratic graphene grown via chemical vapor deposition. *Journal of Applied Physics*, 110(1):013720, 2011.

[132] Andrea C Ferrari. Raman spectroscopy of graphene and graphite: disorder, electron–phonon coupling, doping and nonadiabatic effects. *Solid state communications*, 143(1):47–57, 2007.

[133] Carlos Diaz-Pinto, Debtanu De, Viktor G Hadjiev, and Haibing Peng. Ab-stacked multilayer graphene synthesized via chemical vapor deposition: a characterization by hot carrier transport. *arXiv preprint arXiv:1210.4585*, 2012.

[134] LG Cancado, K Takai, T Enoki, M Endo, YA Kim, H Mizusaki, NL Speziali, A Jorio, and MA Pimenta. Measuring the degree of stacking order in graphite by raman spectroscopy. *Carbon*, 46(2):272–275, 2008.

[135] Joseph A Garlow, Lawrence K Barrett, Lijun Wu, Kim Kisslinger, Yimei Zhu, and Javier F Pulecio. Large-area growth of turbostratic graphene on ni (111) via physical vapor deposition. *Scientific reports*, 6, 2016.

[136] Andrea C Ferrari, JC Meyer, V Scardaci, C Casiraghi, Michele Lazzeri, Francesco Mauri, S Piscanec, Da Jiang, KS Novoselov, S Roth, et al. Raman spectrum of graphene and graphene layers. *Physical review letters*, 97(18):187401, 2006.

[137] Mark Wall. Raman spectroscopy optimizes graphene characterization. *Advanced Materials and Processes*, 170(4):35–38, 2012.

[138] Yufeng Hao, Yingying Wang, Lei Wang, Zhenhua Ni, Ziqian Wang, Rui Wang, Chee Keong Koo, Zexiang Shen, and John TL Thong. Probing layer number and stacking order of few-layer graphene by raman spectroscopy. *small*, 6(2):195–200, 2010.

[139] Seunghyun Lee, Kyunghoon Lee, and Zhaohui Zhong. Wafer scale homogeneous bilayer graphene films by chemical vapor deposition. *Nano letters*, 10(11):4702–4707, 2010.

[140] R Zhang, ZS Wang, ZD Zhang, ZG Dai, LL Wang, H Li, L Zhou, YX Shang, J He, DJ Fu, et al. Direct graphene synthesis on sio2/si substrate by ion implantation. *Applied Physics Letters*, 102(19):193102, 2013.

[141] V. Yu. *Optics and chemical vapour deposition of graphene monolayers on various substrates*. PhD thesis, McGill University Library, 2010.